




# Dual-layer microneedles with NO/O<sub>2</sub> releasing for diabetic wound healing via neurogenesis, angiogenesis, and immune modulation

Changjiang Liu<sup>a,1</sup>, Kun Liu<sup>b,1</sup>, Dong Zhang<sup>a,1</sup>, Yuting Liu<sup>a</sup>, Yifeng Yu<sup>a</sup>, Haifei Kang<sup>b</sup>, Xianzhen Dong<sup>b</sup>, Honglian Dai<sup>b,c,\*</sup>, Aixi Yu<sup>a,\*\*</sup> 

<sup>a</sup> Department of Orthopedics, Zhongnan Hospital of Wuhan University, Wuhan, 430071, PR China

<sup>b</sup> State Key Laboratory of Advanced Technology for Materials Synthesis and Processing, Wuhan University of Technology, Wuhan, 430070, PR China

<sup>c</sup> Wuhan University of Technology Advanced Engineering Technology Research Institute of Zhongshan City, Zhongshan, 528400, PR China

## ARTICLE INFO

### Keywords:

Microneedles  
Gas delivery  
Neurogenesis  
Angiogenesis  
Immune modulation  
Diabetic wounds

## ABSTRACT

Diabetic wounds present multiple functional impairments, including neurovascular dysregulation, oxidative imbalance, and immune dysfunction, making wound healing particularly challenging, while traditional therapeutic strategies fail to address these complex issues effectively. Herein, we propose a strategy utilizing dual-layer microneedles to deliver therapeutic gases by modulating neurovascular coupling and immune functions for diabetic wound treatment. The microneedle can respond to reactive oxygen species (ROS) in the diabetic microenvironment and subsequently generate oxygen (O<sub>2</sub>) and nitric oxide (NO). These gases comprehensively promote neuro-vascular regeneration, reduce oxidative stress levels, and attenuate inflammation. *In vivo* studies demonstrate that the microneedle can accelerate diabetic wound healing by modulating neurovascular regeneration and inflammatory processes. Transcriptomic analyses further validate the involvement of related advantageous signaling pathways. The potential mechanism involves the activation of the PI3K-AKT-mTOR pathway to facilitate autophagy, ultimately accelerating the healing process. Thus, our multifunctional dual-layer microneedles provide an effective strategy for treating diabetic wounds.

## 1. Introduction

With the increasing incidence of diabetes mellitus worldwide, impaired diabetic wound healing has become a significant public health concern [1–3]. Typically, wound healing proceeds through three sequential phases: inflammation, proliferation, and remodeling. However, in diabetic wounds, the healing process is delayed due to multifaceted factors at each phase, including excessive reactive oxygen species (ROS) accumulation, dysautonomia, microcirculatory disturbances, and immune dysregulation [4–7]. High blood glucose levels induce cellular stress and redox imbalance and damage surrounding healthy cells. Impaired blood vessels and nerves reduce oxygen supply and neurotrophic function, further exacerbating the healing process. Additionally, macrophages in diabetic wounds tend to remain in the M1 (inflammatory) phenotype rather than transitioning to the M2 (anti-inflammatory) phenotype, which is crucial for wound repair [8,9]. Ideal

therapeutic strategies should comprehensively address these complex pathophysiological challenges and facilitate various cells, thereby accelerating the healing process.

Among various therapeutic strategies, nerve regeneration has recently garnered significant attention for its role in accelerating tissue repair [10–14], suggesting that its integration with conventional therapeutic strategies, such as ROS clearance, hypoxia amelioration, and macrophage polarization, may provide superior treatment for diabetic wounds. Nonetheless, neurogenesis is an intricate and independent process necessitating the interaction of both neural and non-neural cells, including endothelial cells [15,16]. Consequently, strategies to promote nerve regeneration through the administration of nerve growth factors or electrical stimulation often yield suboptimal outcomes, mainly due to the insufficient emphasis on the neurovascular coupling effect. Additionally, their operational complexity and high costs limit their clinical applicability. Hence, a feasible multifunctional material is needed to

\* Corresponding author. State Key Laboratory of Advanced Technology for Materials Synthesis and Processing, Wuhan University of Technology, Wuhan, 430070, PR China.

\*\* Corresponding author.

E-mail addresses: [daihonglian@whut.edu.cn](mailto:daihonglian@whut.edu.cn) (H. Dai), [yuaixi@whu.edu.cn](mailto:yuaixi@whu.edu.cn) (A. Yu).

<sup>1</sup> Changjiang Liu, Kun Liu, and Dong Zhang contributed equally to this work.

<https://doi.org/10.1016/j.bioactmat.2024.12.012>

Received 9 October 2024; Received in revised form 20 November 2024; Accepted 10 December 2024

2452-199X/© 2024 The Authors. Publishing services by Elsevier B.V. on behalf of KeAi Communications Co. Ltd. This is an open access article under the CC BY-NC-ND license (<http://creativecommons.org/licenses/by-nc-nd/4.0/>).

improve the functions of various cells in the wound microenvironment and promote nerve regeneration, thereby further expediting the healing process.

Gas therapy strategies are noted for their simplicity and safety, as gas molecules are integral to numerous biological processes [17]. This has garnered considerable interest in the field of regeneration, particularly regarding the roles of nitric oxide (NO) and oxygen (O<sub>2</sub>). In diabetic wounds, however, levels of NO and O<sub>2</sub> are often deficient, and closely associated with poor healing outcomes [18–20]. NO mediates a multitude of biological activities, including neuromodulation, vascular homeostasis, and immune responses. Previous studies have shown that NO delivery can promote angiogenesis and regulate macrophage polarization, thereby enhancing wound repair [21,22]. Recent research further indicates that NO can facilitate peripheral nerve repair, suggesting its potential to promote nerve regeneration in diabetic wounds, an aspect that has been overlooked in previous studies, as one of the primary causes of diabetic wounds is neuropathy [23,24]. Similarly, due to vascular damage in diabetes, hypoxia in the deeper wound layers impedes cell fate, including proliferation and migration. Exogenous O<sub>2</sub> delivery is clinically applied for diabetic wound healing through cumbersome hyperbaric methods to improve tissue hypoxia and cellular function [25]. Therefore, combined therapy with NO and O<sub>2</sub> holds significant promise for synergistically enhancing the cellular function within the wound microenvironment and regulating neurovascular and

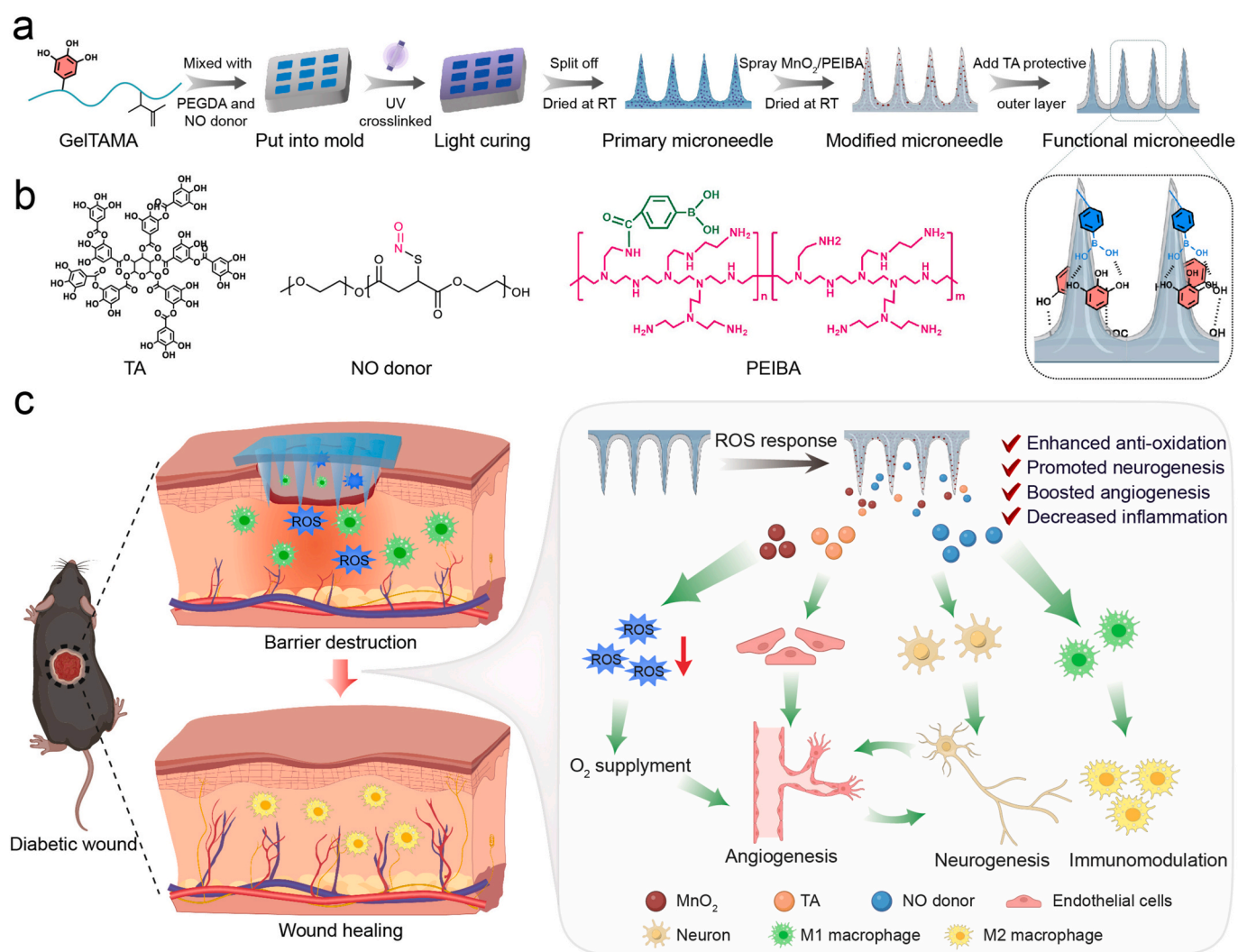
immune responses, thereby systematically improving the healing process of diabetic wounds.

Microneedles, which can penetrate dermal tissue with minimal invasiveness, offer a promising method for delivering therapeutic agents, including drugs, therapeutic gases, and nanoparticles [26–31]. Herein, we designed a dual-layer multifunctional microneedle capable of generating O<sub>2</sub> and NO intelligently, leveraging the microneedle's properties to deliver gases deep into the skin (Scheme 1). The sustained release of O<sub>2</sub> and NO activated beneficial signaling pathways, promoting neurogenesis and angiogenesis, as well as the polarization of macrophages to the M2 phenotype, thereby accelerating wound healing in diabetic mice. This design introduces the concept of supportive neurogenesis-angiogenesis and immune regulation throughout the healing process by delivering therapeutic gases directly using multifunctional microneedles, with the significant potential for further clinical application in diabetic wounds.

## 2. Materials and methods

### 2.1. Materials

Gelatin was sourced from Sigma-Aldrich, USA. Tannic acid and polyethyleneimine (PEI) were purchased from Aladdin Industrial Corporation, China. Manganese dioxide (MnO<sub>2</sub>) was obtained from Jin Cai



**Scheme 1.** Schematic illustration of the multifunctional microneedles for diabetic wound healing. a) Preparation process of microneedle. b) Structural formula of the main ingredients. c) Mechanism of promoting wound healing via neurovascular immune modulation by multi-functional microneedle.

Xin Materials Co., Ltd., China. Poly (ethylene glycol) diacrylate (PEGDA), with a molecular weight of 500, was acquired from Aladdin Industrial Corporation, China. Lithium phenyl(2,4,6-trimethylbenzoyl) phosphinate (LAP) was procured from Aladdin Industrial Corporation, China. Maleic anhydride was also purchased from Aladdin Industrial Corporation, China.

## 2.2. Synthesis of GelTAMA

Gelatin-Tannic Acid (GelTA) and its modified form, Gelatin-Tannic Acid-Maleic Anhydride (GelTAMA), were synthesized through a series of well-defined steps. Initially, 1 g of gelatin was dissolved in 10 mL of deionized water to prepare a 10 % (w/v) solution, heated, and adjusted to pH = 8.5 with 0.1 M NaOH before 0.05 g of tannic acid (5 % of the gelatin mass) was introduced in 1 mL of water to form GelTA. After adjusting the pH to 7.4, the mixture underwent a reaction for 3 h, followed by dialysis and lyophilization to form a stable dry powder. Subsequently, this precursor (1 g) was dissolved in 10 mL of PBS at 40 °C, to which 0.5 mL of maleic anhydride was added, and the mixture was reacted for 6 h. The reaction mixture was then enhanced with an additional 5 mL of PBS, dialyzed for three days, and lyophilized again to produce GelTAMA. The <sup>1</sup>H NMR spectra of the GelTAMA were recorded using an AMX-500 NMR spectrometer (Bruker, Germany), with D<sub>2</sub>O serving as the solvent. Fourier-transform infrared (FTIR) spectroscopy was used to analyze the chemical groups of Gel, GelTA, and GelTAMA, with a scanning range of 500–4000 cm<sup>-1</sup>.

## 2.3. Synthesis of PEIBA

PEIBA was synthesized according our previous study [32], 5 g of a 50 % w/w aqueous polyethylenimine (PEI) solution was dissolved in 20 mL of deionized water, ensuring uniform mixing. Subsequently, 2.04 g of 4-carboxyphenylboronic acid was added, and the solution's pH was adjusted to 5.5 using hydrochloric acid (HCl) to facilitate the chemical reaction. The reaction was then activated by adding 3.03 g of 1-ethyl-3-(3-dimethylaminopropyl) carbodiimide hydrochloride (EDC) and 2.11 g of N-hydroxysuccinimide (NHS), and allowed to proceed under stirring for 18 h. After the reaction, the mixture was dialyzed against deionized water to remove any unreacted reagents and byproducts, followed by freeze-drying to obtain PEIBA as a dry powder. The lyophilized product was stored in sealed vials at low temperatures to maintain stability and prevent degradation. The <sup>1</sup>H NMR spectra of the PEIBA were recorded using an AMX-500 NMR spectrometer, with D<sub>2</sub>O serving as the solvent.

## 2.4. Synthesis of NO donor

**Initial Reaction Setup:** Weigh 2 g of mPEG (Polyethylene glycol monomethyl ether) and 1 g of mercaptosuccinic acid into a 100 mL dry round-bottom flask. Add 0.16 g of PTSA (p-Toluenesulfonic acid monohydrate) 0.16 g of EDTA (ethylenediaminetetraacetic acid), and 372 μL of ethylene glycol. Perform three vacuum/nitrogen cycles to ensure an anhydrous and oxygen-free environment. Heat the mixture under an argon atmosphere at 120 °C for 8 h, removing water vapor during the reaction.

**Post-reaction Processing:** Dissolve the hot reaction mixture in 25 mL of acetone. Precipitate the polymer by adding the solution to ice-cold diethyl ether. Repeat this process three times to thoroughly remove impurities. Filter the precipitated solid and dry under vacuum for 4 h, yielding the precursor polymer mPEG-P(MS-EG). This product is the precursor polymer mPEG-P(MS-EG).

**Nitrosation Reaction:** Dissolve 0.5 g of the precursor mPEG-P(MS-EG) in 20 mL of anhydrous methanol with ultrasonication and stirring. Subsequently, add 240 μL of tert-butyl nitrite to initiate the nitrosation process. To enhance solubility, introduce 5 mL of chloroform to the mixture. After 2 h, the red color indicates reaction completion.

Pour the mixture into 400 mL of pre-cooled anhydrous diethyl ether to precipitate the product. Store at -20 °C, filter, and dry the solid under vacuum to obtain a pink or red final product.

## 2.5. Preparation of Microneedle@NO

Dissolve 1 g of GelTAMA in 5 mL of PBS at 60 °C to form a 20 % (w/v) solution. Add 1 mg of a NO donor and 20 μL of PEGDA to the solution. Introduce 2.5 mg of LAP (Lithium phenyl-2,4,6-trimethylbenzoylphosphinate) to the mixture. Use ultrasonication to ensure thorough mixing of all components. Pour the mixture into a microneedle mold. Apply repeated vacuum cycles to remove air bubbles and ensure the mold was completely filled. Then concentrate to dryness in a vacuum oven with repeated additions of the solution, and finally cure the microneedles under 405 nm UV light to initiate polymerization and form a stable structure. The reaction product of GelTAMA and PEGDA was characterized using FTIR, with a scanning range of 500–4000 cm<sup>-1</sup>.

## 2.6. Preparation of Microneedle@NO@MnO<sub>2</sub>

Dissolve 0.1 g of PEIBA in 5 mL of PBS. Add 0.5 mg of MnO<sub>2</sub> and ultrasonicate the solution to achieve a uniform dispersion. Spray the MnO<sub>2</sub> solution onto the surface of the prepared microneedles. Allow the coated microneedles to air dry in a well-ventilated area. Subsequently, apply a 10 % tannic acid (TA) solution by spaying to the microneedles to form a protective outer layer.

## 2.7. Characterization of MnO<sub>2</sub> and NO donor

The <sup>1</sup>H NMR spectra of the NO precursor and donor were recorded using an AMX-500 NMR spectrometer (Bruker, Germany), with D<sub>2</sub>O serving as the solvent.

The micromorphology of MnO<sub>2</sub> was characterized by TEM (FEI Tecnai F20, America) and SEM (TESCAN MIRA LMS, Czech Republic), the zeta potential and Dynamic light scattering (DLS) and zeta potential were measured at 25 °C on a Zetasizer Nano ZS90 analyzer (Malvern Instrument Ltd, UK). The micromorphology of NO precursor and donor was characterized by TEM (FEI Tecnai F20, America).

## 2.8. Characterization of microneedle

The microscopic morphology of microneedles and microneedles after compression was characterized using SEM. The adhesive performance of the microneedles was assessed by first adhering them to pig skin and compressing them for 2 min. Subsequently, a tensile test was conducted at a speed of 1 mm/min using a mechanical testing machine (MTS, America). The swelling properties of microneedles were evaluated by the weighing method after immersion in PBS solution for 0, 0.5, 1, 2, 4, 6, and 8 h. The swelling rate was calculated as follows:

$$S = \frac{W_b - W_a}{W_a}$$

W<sub>a</sub> is the initial freeze-dried mass; W<sub>b</sub> is the microneedles weight after swelling. To investigate the release of NO from Microneedle@NO, the NO concentration in the solution at different times (1 d, 2 d, 3 d, 4 d, 5 d, 6 d, and 7 d) was detected using Griess reagent (S0021S, Beyotime Biotechnology) at room temperature.

## 2.9. Cell viability, proliferation, and apoptosis

All cells were purchased from Procell Corporation (Wuhan, Hubei, China). L929 cells were seeded in 96-well plates (5 × 10<sup>3</sup> cells/well) and 6-well plates (1 × 10<sup>5</sup> cells/well) cultured by MEM medium supplemented with 10 % fetal bovine serum (FBS, Gibco) and 1 % P/S in 5 % CO<sub>2</sub> incubator. To evaluate the cytotoxicity, we performed CCK-8, live/

dead staining, and Annexin V-FITC/PI apoptosis detection. After incubation for 24 h, we replaced the medium with a new medium containing 50 % (v/v) steep liquor in 96-cell plates. The CCK-8 assays were applied to analyze cell viability in 1, 2, and 3 days. Briefly, after removing the supernatants, 100  $\mu$ L medium contain 10 % (v/v) CCK-8 solution was added and further incubated for 2 h. The optical density (OD) at 450 nm was read (Multiskanfc, Thermo Scientific) and cell viability was calculated by the formula: cell viability (%) = [(OD<sub>sample</sub> - OD<sub>blank</sub>)/(OD<sub>control</sub> - OD<sub>blank</sub>)].

In 6-well plates, we directly co-culture the cells with materials. In live/dead staining, cells were treated with 1 mM Calcein-AM/2 mM PI working solution for 45 min in the dark and recorded in a fluorescence microscope. To evaluate apoptosis/necrosis, the L929 cells were harvested after incubation for 3 days, then stained with Annexin V-FITC/PI apoptosis detection kit (Elabscience, Wuhan, China) strictly according to the manufacturer instructions. The stained cells were further detected by flow cytometry (FC500, Beckman Coulter, Fullerton, CA, USA).

### 2.10. Anti-oxidation performance, oxygen generation and nitric oxide releasing evaluation in cells

Human umbilical vein cells (HUVECs) and pheochromocytoma (PC12) cells were seeded in a 6-well plate ( $1 \times 10^5$  cells/well) to evaluate the anti-oxidation ability. HUVECs were cultured in Endothelial Cell Medium (ECM, Scien Cell) with endothelial cell growth supplement (ECGS), 10 % FBS and 1 % P/S. PC12 cells were cultured with RPMI-1640 with 10 % horse serum (HS) and 1 % P/S. After incubation for 24 h under a hypoxic atmosphere (1 % O<sub>2</sub>), the tailor-made materials (5 mm  $\times$  5 mm) were placed in the center and a medium containing 100  $\mu$ M H<sub>2</sub>O<sub>2</sub> was added.

The ROS scavenging ability was investigated by a DCFH-DA (dichloro-dihydro-fluorescein diacetate) probe kit (Solarbio, Beijing, China). Briefly, after 3 days, DCFH-DA solution (10  $\mu$ M) was added to the supernatant and incubated for 20 min. In addition, the O<sub>2</sub> indicator Ru(dpp)<sub>3</sub>Cl<sub>2</sub> kit (BestBio, China) and NO indicator DAF-FM DA kit (Solarbio) were performed to detect the intercellular O<sub>2</sub> production and NO release strictly following the instructions. The fluorescence images were recorded by fluorescence microscope and the quantitative data was further obtained using flow cytometry analysis.

### 2.11. In vitro neurite outgrowth evaluation

PC12 cells were seeded in the 24-well plate ( $1 \times 10^4$  cells/well). Simultaneously, the medium containing 100  $\mu$ M H<sub>2</sub>O<sub>2</sub> and 10 ng mL<sup>-1</sup> NGF was employed to mimic the inflammatory environment and induce PC12 cell differentiation. Samples were sterilized with 70 % ethanol, washed with PBS three times, exposed to ultraviolet light for 2 h, and further placed in the upper chamber to co-culture with PC12 cells.

Following the cell culture for 3 days, cell morphology was investigated to evaluate neurite outgrowth. Briefly, cells were fixed with 4 % w/v paraformaldehyde for 20 min and washed three times with PBS. Then 0.5 % v/v Triton X-100 was used for permeabilization for 5 min. Next, cells were washed with PBS and incubated in the 100 nM Rhodamine-Phalloidin (Solarbio) working solution for 30 min. After incubation, the nuclei were further stained with SYROX Green (Invitrogen). The images were recorded with confocal laser scanning microscopy (CLSM; TCS SP8, Leica, Germany). The acquired images were analyzed with ImageJ software. The differentiation degree was evaluated according to the ratio of the cell body and the length of neurite (L0, L1, and L2).

### 2.12. Proliferation, migration and angiogenesis of HUVECs

HUVECs were seeded on the 24-well plate ( $1 \times 10^4$  cells/well). 5-ethynyl-2'-deoxyuridine (Edu) assay kit (Beyotime Biotechnology, China) was used to detect proliferation. Briefly, cells were incubated

with 10  $\mu$ M edu working solution for 2 h. Then, fixation and permeabilization were successively conducted by 4 % w/v paraformaldehyde for 15 min and 0.3 % v/v Triton X-100 for 15 min, following cells were washed with PBS containing 3 % v/v Bovine serum albumin (BSA). Cell nuclei were stained by hoechst33342 for 10 min. In migration assay, when HUVECs converged to 90 %, FBS-free was used to induce starvation for 24 h. Then a straight line was scratched by a sterile 200- $\mu$ L pipette tip. Plates were washed by PBS and replenished new medium containing 1 % FBS and the upper chamber containing tailored samples. Cells were photographed at 0 h and 48 h and scratches were quantitatively investigated using ImageJ. The migration rate was calculated via the formula: Scratch wound area (%) = (A<sub>48h</sub>/A<sub>0h</sub>)  $\times$  100, A means the scratch area. In angiogenesis assays, 100  $\mu$ L pre-cooled diluted Matrigel (BD Biosciences, CA, USA) 10 % v/v in ECM complete medium was added in 24-well plated to coat. Then HUVECs ( $1 \times 10^4$  cells/well) were seeded and incubated with a medium containing 100  $\mu$ M H<sub>2</sub>O<sub>2</sub> and samples in the upper chamber. After 3 days, HUVECs were stained by Rhodamine-Phalloidin and SYROX Green same as above. Capillary-like tube formation was recorded by CLSM. In the tube-forming assay,  $3 \times 10^4$ /well HUVECs were added into 96-well plated and incubated with Matrigel for 6 h. Then capillary-like structure formation was observed with an optical microscope.

### 2.13. Interaction of Co-culture of PC12 cells and HUVECs

In the direct co-cultured model, HUVECs ( $5 \times 10^3$  cells/well) were first seeded in the lower chamber. After 24 h, PC12 cells ( $1 \times 10^4$  cells/well) were added and further co-cultured for 10 days. Then cells were collected and investigated. In immunofluorescence, briefly, cells were fixed and permeabilized as above. 10 % v/v goat serum was applied for blocking for 30 min. Then, cells were incubated with primary antibodies (Rabbit anti- $\beta$ -tubulin III and mouse anti-CD31 1:1,000, Abcam, UK) at 4 °C overnight. Next, relevant secondary antibodies (1:1000, Abcam) were added at room temperature and incubated for 1 h. Cell nuclei were stained with hoechst33342 for 10 min.

### 2.14. Evaluation of immunomodulatory performance

RAW264.7 cells were plated at a density of  $5 \times 10^5$  cells in 6-well transwell plates in MEM medium supplemented with 10 % FBS and 1 % P/S. To induce M1 polarization, the cells were initially stimulated with 100 ng/mL lipopolysaccharide (LPS, Solarbio) and 10 ng/mL interferon- $\gamma$  (IFN- $\gamma$ , Solarbio) for 24 h. Then, the medium was replaced and samples were placed in the upper chamber for 48 h. Next, M2 macrophages were detected by immunofluorescence and cytometry analysis. The procedures were the same as above and the primary antibodies were mouse anti-CD206 and mouse anti-Arg1 (1:1000, Abcam). In cytometry detection, briefly, cells were harvested and incubated with FcR block solution (BioLegend, Australia) at 4 °C for 10 min. Then, cells were stained with anti-CD86 FITC (1:100, BioLegend) working solution, further fixed with fixation buffer (BioLegend) for 30 min at room temperature, and permeabilized by intracellular staining permeabilization Buffer (BioLegend). Next, cells were incubated with anti-CD206 APC (1:100, BioLegend) working solution for 30 min, further detected by flow cytometry (Beckman).

### 2.15. Gene expression assays and protein expression detection

Relative mRNA expression level was investigated by quantitative reverse transcription polymerase Chain Reaction (RT-qPCR) and protein expression was analyzed by Western blotting. In neurite outgrowth evaluation, we examined the expression level of marker genes (BDNF, TrkB, and Tubulin) and proteins (NF, GAP43; 1:1000, Abcam). In the HUVECs, we detected the expression level of protein (CD31, 1:1000, Abcam). In the co-culture system, the expression level of marker genes (BDNF, TrkB, VEGF, and VEGFR2) were tested. In macrophage

polarization assays, M2 macrophage polarization were examined by detecting the expression level of proteins (Arg-1 and CD206, 1:1000, Abcam). *In vivo* Test, we detected the expression level of marker genes (Tnf, Il1b, Robo2, Sema3c, and Vegfa) and proteins (mTOR, p-mTOR, Abcam; PI3K, p-PI3K, Abclonal; AKT, p-AKT, CST).

## 2.16. *In vivo* test

C57BKS *db/db* spontaneously diabetic mice (6–8 weeks) were used to investigate wound healing and randomly divided into four groups. 1 % sodium pentobarbital saline solution was applied for anesthesia through intraperitoneal. The 8 mm diameter skin defects on the back were created without tension and fixed by a sterile perforated patch. Different microneedles were used to cover the wound and replaced every 3 days. Digital photos of the wound were captured at predetermined intervals. Residual wound area rate was calculated by the formula: Residual wound area rate (%) =  $[A_{\text{residual}}/A_{\text{original}}] \times 100$ ; A represents area. On day 10, mice in the control and ideal material groups were sacrificed for detecting transcriptome sequencing of wound tissues. On day 14 post

wounding, diabetic mice were sacrificed and wound tissues were collected for further investigation. Hematoxylin and Eosin (H&E) and Masson's trichrome staining were conducted to evaluate tissue regeneration. Immunofluorescence was stained to examine nerve regeneration, vessel formation, and immune infiltration. The marker protein expression was also detected including NF,  $\alpha$ -SMA, and CD31. Meanwhile, *in vivo* biocompatibility of microneedles was investigated in diabetic mice. The heart, lung, liver, spleen, and kidney were harvested and processed via H&E staining analysis. To assess the mechanism of the microneedle on diabetic wound healing, skin tissues were harvested on day 10 post-operation for transcriptome sequencing gene expression analysis, protein expression evaluation, and biological transmission electron microscopy (HT7700, Hitachi, Japan).

## 2.17. Statistical analysis

Unless otherwise stated, all results were statistically analyzed and reported as mean  $\pm$  standard deviation. A one-way analysis of variance with Turkey's post hoc test was conducted for sample analyses. The

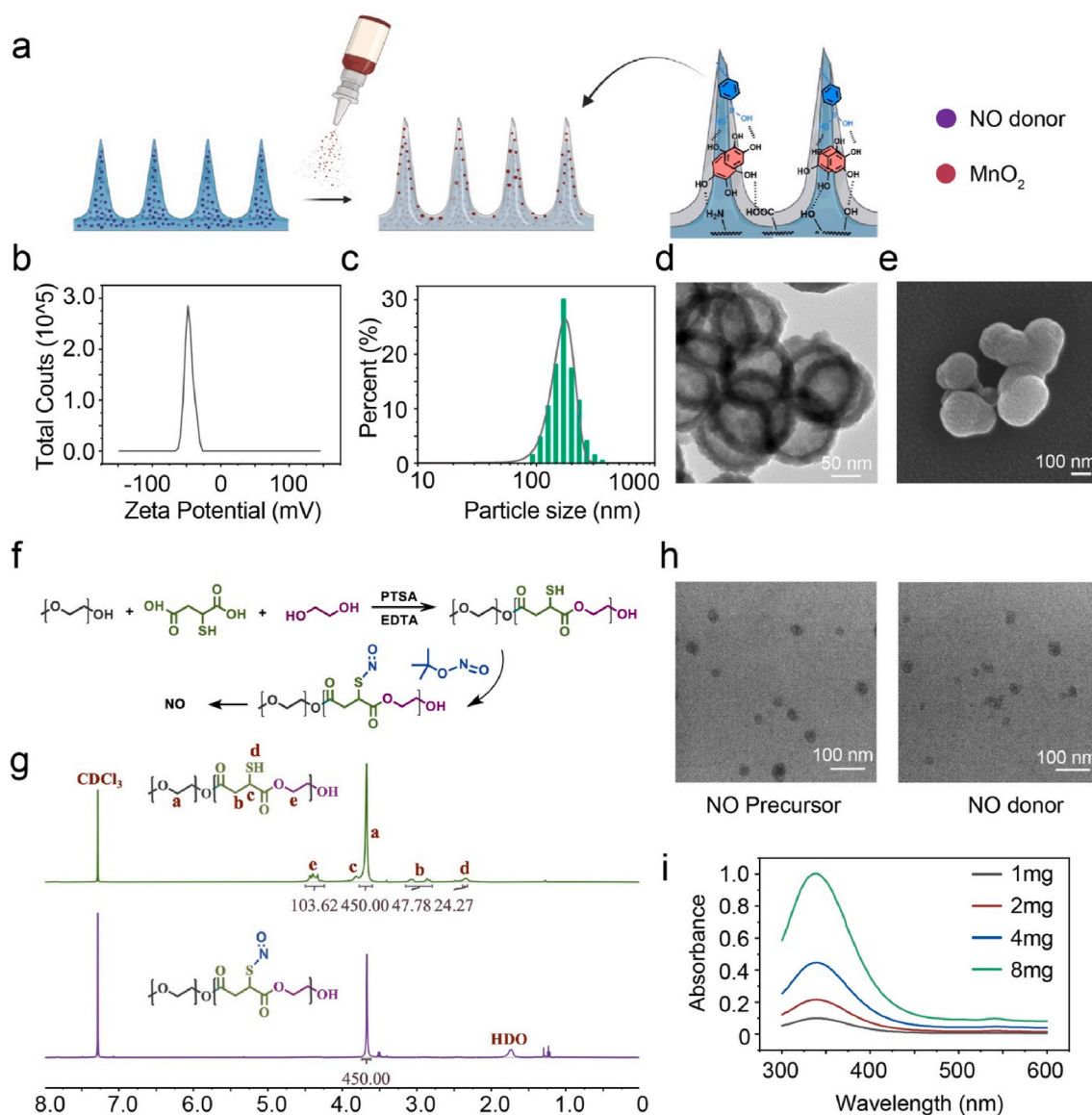


**Fig. 1.** Synthesis and characterization of MnO<sub>2</sub> and NO donor. a) Schematic diagram of MnO<sub>2</sub> and NO donor used in the microneedle fabrication process. The zeta potential b) and DLS measurement c) of MnO<sub>2</sub>. The TEM d) and SEM e) images of MnO<sub>2</sub>. f) Reaction scheme for the preparation of the NO donor. g) NMR analysis of the NO precursor and donor. h) TEM images of the NO precursor and donor. i) UV absorption peaks of NO release at different concentrations.

difference was considered significant at  $p < 0.05$ . \* $p < 0.05$ , \*\* $p < 0.01$ , \*\*\* $p < 0.001$ , n.s. no significance.

### 3. Results and discussion

#### 3.1. Fabrication and characterization of microneedles

In this study, we designed a dual-layered microneedle system

capable of gradient gas release. As depicted in Fig. 1a, the inner layer contains an NO donor, which releases nitric oxide (NO) through S-N bond dissociation. The S-N bond in S-nitrosothiol is relatively unstable and readily dissociates under physiological conditions (such as ROS, light, and heat), releasing NO. By embedding RSNO into a macromolecular matrix, its stability is enhanced, effectively delaying NO release and preventing premature dissociation. The outer layer is coated with manganese dioxide ( $\text{MnO}_2$ ), which reacts with hydrogen peroxide

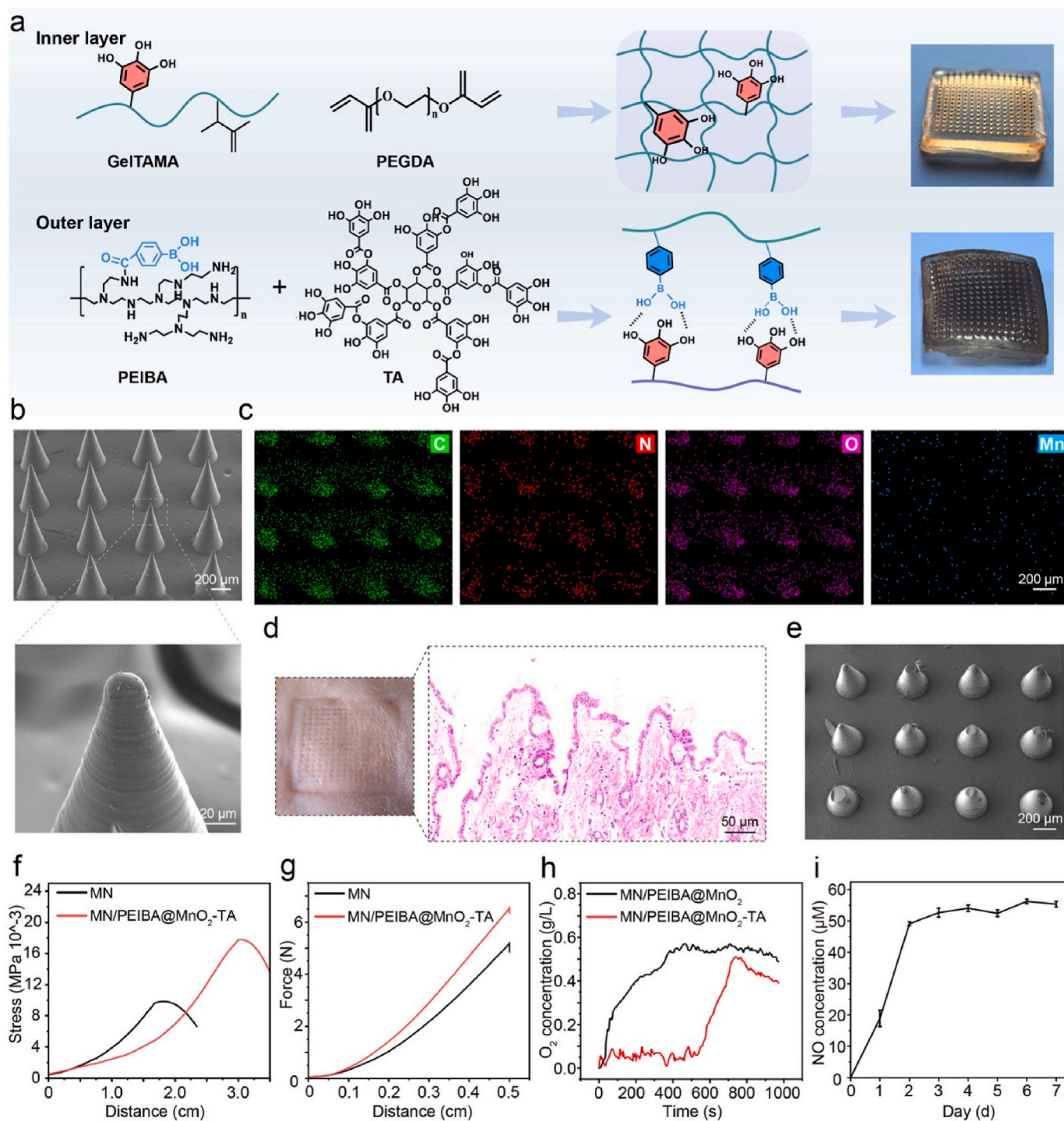


**Fig. 2.** Synthesis and characterization of the functional microneedle. a) Reaction scheme for the inner and outer layers. b) SEM analysis of the functional microneedles after spraying. c) Surface elemental analysis of functional microneedles. d) Microneedle penetration into the skin and H&E staining. e) SEM analysis of the microneedles. The adhesion strength f) and mechanical strength g) of the microneedles. The O<sub>2</sub> h) and NO i) release from the microneedles (n = 3). Data are represented as mean values ± SD.

(H<sub>2</sub>O<sub>2</sub>) to release oxygen, facilitating a controlled and synergistic gas delivery. Detailed analyses were conducted on both MnO<sub>2</sub> and the NO donor. The zeta potential measurement of MnO<sub>2</sub> indicated a value of approximately  $-50$  mV (Fig. 1b), suggesting good dispersibility of MnO<sub>2</sub>. Dynamic Light Scattering (DLS) showed that the average size of the MnO<sub>2</sub> particles was around 200 nm (Fig. 1c). Transmission Electron Microscopy (TEM) and Scanning Electron Microscopy (SEM) images (Fig. 1d and e) revealed that MnO<sub>2</sub> possessed a hollow spherical structure, and the size was consistent with the DLS result.

The NO donor was synthesized using our previously established method (Fig. 1f), with its successful creation confirmed through Nuclear Magnetic Resonance (NMR) analysis (Fig. 1g). TEM analysis demonstrated that the NO donor particles were approximately 10 nm in size (Fig. 1h). Additionally, these particles exhibited a distinct absorption peak at 330 nm in the ultraviolet spectrum, indicating the presence of NO (Fig. 1i; Fig. S1).

The microneedles were fabricated through a two-step process, as depicted in the scheme (Fig. 2a). Initially, the inner layer was formed by adding Gelatin-Tannic Acid-Maleic Anhydride (GelTAMA), Poly (ethylene glycol) diacrylate (PEGDA), and the NO donor into a mold. GelTAMA was obtained by grafting tannic acid (TA) and methacrylic anhydride onto gelatin. After gelatin was grafted with TA, due to the electron-withdrawing effect of the phenolic hydroxyl group, the carbonyl (C=O) peak shifted from 1653 cm<sup>-1</sup>–1643 cm<sup>-1</sup>, and the hydroxyl (-OH) peak shifted from 3421 cm<sup>-1</sup>–3404 cm<sup>-1</sup>. Subsequent grafting of the double bond caused the carbonyl (C=O) peak to shift again to 1648 cm<sup>-1</sup>, and introduced a C-H stretching vibration peak of the methyl group (-CH<sub>3</sub>) in methacrylic anhydride at 2851 cm<sup>-1</sup>. (Fig. S2). Furthermore, NMR spectroscopy indicated that the double bond groups were successfully grafted onto GelTAMA (Fig. S3). The vacuum was applied to fill the mold's bottom with the mixture, followed by a continued vacuum to compact the solution. After UV exposure, the microneedles were carefully demolded. Compared to GelTAMA, GelTAMA-PEGDA exhibited a characteristic peak at 1103 cm<sup>-1</sup>, corresponding to the ether bond in PEGDA, and a methylene peak at 2940 cm<sup>-1</sup> (Fig. S4). These findings confirmed that PEGDA successfully reacted with GelTAMA. Concurrently, a MnO<sub>2</sub> solution prepared with 4-Carboxyphenylboronic acid-grafted PEI (PEIBA) and TA was used for coating. PEIBA was obtained by the previous method [32], and its NMR spectrum was shown in Fig. S5. PEIBA and TA reacted to form borate ester bonds, and a new characteristic peak of 1502 cm<sup>-1</sup> appears in the infrared spectrum (Fig. S6). The microneedles were first sprayed with the PEIBA@MnO<sub>2</sub> solution, followed by a layer of TA solution, and then dried in a vacuum environment. Before coating, the microneedles appeared yellow, the color of GelTAMA, which turned black after coating due to the presence of MnO<sub>2</sub>. SEM analysis revealed that the surface of the MnO<sub>2</sub>-coated microneedles became granular (Fig. 2b), in contrast to the surface of uncoated microneedles (Fig. S7). Elemental analysis by EDS indicated a uniform distribution of C, N, and O elements across the microneedles, with a lower concentration of Mn, which was not aggregated on the microneedles (Fig. 2c). The microneedles left clear marks on the skin upon application, and H&E staining demonstrated successful penetration of the skin (Fig. 2d). Macroscopic observations revealed that these marks largely disappeared within 24 h after the microneedles were removed from the skin (Fig. S8). SEM analysis showed slight breakage of microneedles (Fig. 2e). Furthermore, texture analysis and adhesion testing revealed that the adhesive properties and mechanical penetration force of the microneedles were enhanced after coating (Fig. 2f and g). This improvement was attributed to the interactions between the polyphenol groups of PEIBA, GelTAMA, and TA, which bolstered the mechanical integrity. The outer layer of TA contained effective adhesive groups that could form strong bonds with amino, carboxyl, and hydroxyl groups present on the skin.

Concurrently, the reaction between nanoscale MnO<sub>2</sub> and hydrogen peroxide was observed to produce a significant release of O<sub>2</sub>, underscoring the functional efficacy of the designed microneedle system in

mediating controlled gas release for potential therapeutic applications. Further analysis was conducted on the O<sub>2</sub> release capabilities of the microneedles, as depicted in Fig. 2h. Upon application of the MnO<sub>2</sub>-laden PEIBA solution, a rapid release of O<sub>2</sub> was observed. Following the application of the TA solution, O<sub>2</sub> release was delayed, indicating the responsive nature of the PEIBA-TA layer. This delay was due to the exposure of MnO<sub>2</sub> in the presence of H<sub>2</sub>O<sub>2</sub>, which then reacted further with H<sub>2</sub>O<sub>2</sub> to release O<sub>2</sub>. This mechanism ensured the therapeutic release of oxygen in severely compromised immune environments at the wound site while preserving MnO<sub>2</sub> under normal conditions. Moreover, NO was released continuously for more than three days, with an average release of 18.89 μM on the first day, 49.17 μM on the second day, and 52.67 μM on the third day, ultimately maintaining a constant concentration in the solution (Fig. 2i). Swelling tests indicated that the addition of various materials did not significantly affect the swelling of the microneedles, suggesting the structural stability of the microneedle formulation under physiological conditions (Fig. S9). When the microneedles came into contact with the imbalanced redox environment within the wound, the binding between PEIBA and TA broke down, exposing MnO<sub>2</sub>, which reacted with H<sub>2</sub>O<sub>2</sub> to produce O<sub>2</sub>. This cascade further led to the degradation of the PEIBA layer and the release of NO gas, ultimately achieving the gradient release of both gases.

### 3.2. Biocompatibility of microneedles

Excellent biocompatibility is a fundamental requirement for medical functional materials. In our study, we utilized L929 fibroblast cells, commonly employed to evaluate the biosafety of therapeutic materials for wound healing [33]. The microneedles containing different components were abbreviated as MN (microneedles alone), MN-O<sub>2</sub> (microneedles with MnO<sub>2</sub>), and MN-O<sub>2</sub>/NO (microneedles with MnO<sub>2</sub> and NO donor). As shown in Fig. 3a, all groups treated with different microneedles extracts exhibited cell viabilities exceeding 90 %, indicating the nontoxicity of the microneedles. Additionally, we assessed the compatibility of the microneedles through direct co-culture to prevent overlooking cytotoxic effects. In live/dead staining assays, almost no dead cells marked by red fluorescence were observed at 1, 2, and 3 days (Fig. 3b). Furthermore, we collected L929 cells to conduct flow cytometric (FCM) detection for evaluating necrosis and apoptosis. The results showed no significant difference between the control group and microneedle-treated groups, confirming the superior biocompatibility of microneedles (Fig. 3c; Fig. S10).

### 3.3. H<sub>2</sub>O<sub>2</sub>-activated nitric oxide and oxygen generation of microneedles

Wound healing is a continuous, stepwise biological process that relies on proper redox homeostasis. However, diabetic wounds often exhibit excessive accumulation of ROS, leading to delayed or non-healing wounds [34]. To circumvent the problem, various strategies have been developed to scavenge ROS, including doping with antioxidant molecules or biocatalytic nanostructures [35]. Among all kinds of ROS, H<sub>2</sub>O<sub>2</sub> is the most abundant in diabetic wounds, offering a potential therapeutic target as it can be catalyzed by nano-enzymes to produce oxygen [36]. Here, we developed an intelligently responsive microneedle capable of eliminating H<sub>2</sub>O<sub>2</sub> and producing oxygen and nitric oxide in high ROS environments. To demonstrate the ROS scavenging and oxygenation capability, assays were performed in two kinds of ROS-sensitive cells, including nerve cells (PC12) and human umbilical vascular endothelial cells (HUVECs). The control group was treated with PBS, while the experimental groups were treated with a medium containing 100 μM H<sub>2</sub>O<sub>2</sub> and further incubated under hypoxic conditions to stimulate the hostile microenvironment of diabetic wounds. In contrast, the untreated group only consisted of cells incubated under normal conditions without H<sub>2</sub>O<sub>2</sub> exposure. As shown in Fig. 3f, the green fluorescence intensity, which indicated ROS levels, slightly decreased in the MN group due to the phenylborate ester bond's destruction by high ROS

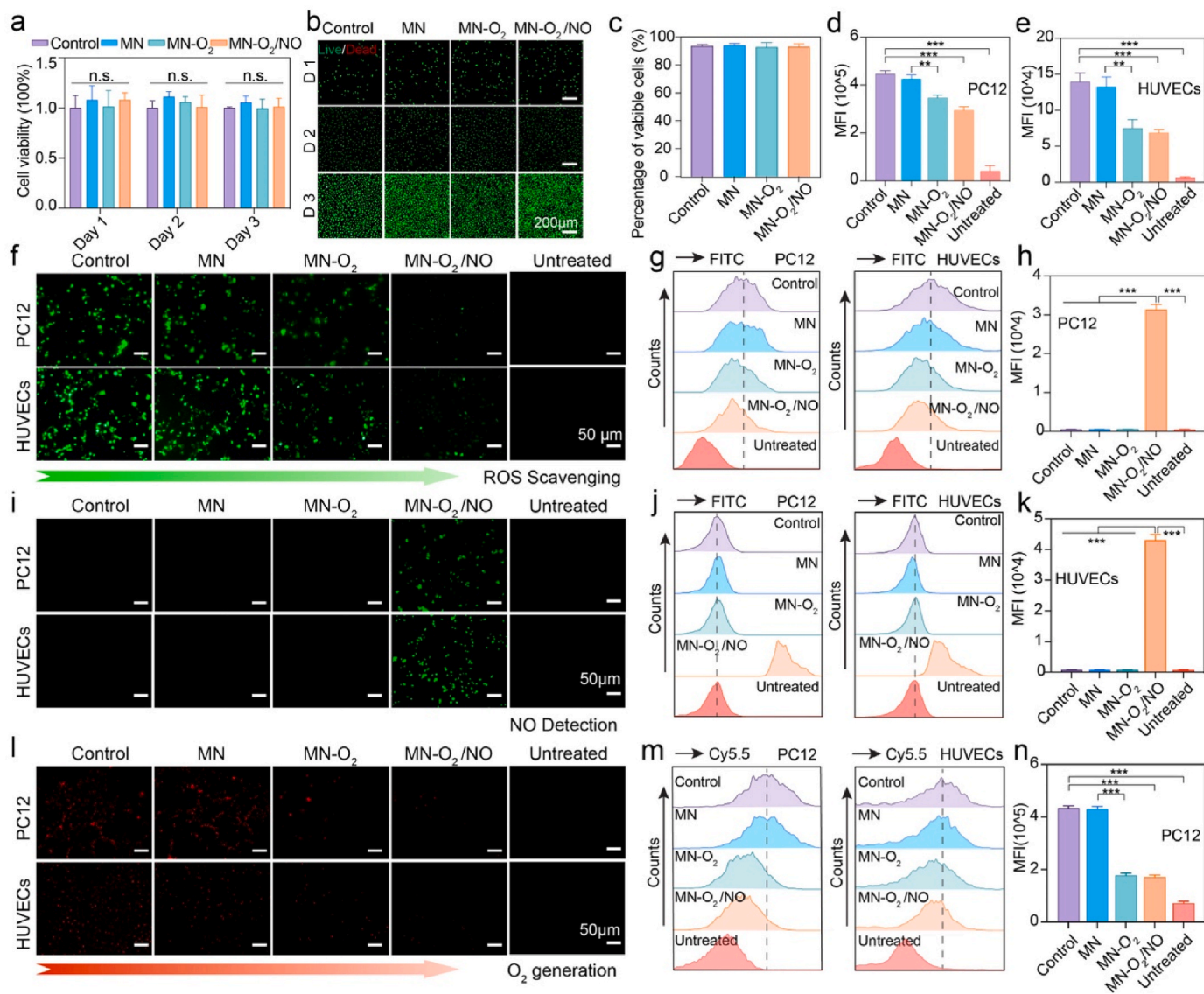


**Fig. 3.** *In vitro* evaluation of the biocompatibility and the capability of microneedle to scavenge ROS and generate NO and O<sub>2</sub>. The cell viability of L929 cells assessed by CCK-8 assay a), Calcein AM/PI staining b), and FCM of Necrosis-apoptosis c). d) and e) Quantitative analyses of MFI for ROS scavenging. Represent fluorescent staining for DCFH-DA f), DAF-FM i), and Ru(dpp)<sub>3</sub>Cl<sub>2</sub> l) in PC12 cells and HUVECs. FCM results for ROS scavenging g), NO-release j), and O<sub>2</sub> generation m). Quantitative analyses of MFI for NO release h, k), and O<sub>2</sub> generation n). Data are represented as mean values ± SD.

and the antioxidant role of TA [37]. Notably, the MN-O<sub>2</sub> and MN-O<sub>2</sub>/NO groups exhibited a significant decrease in green fluorescence intensity, manifesting an enhanced H<sub>2</sub>O<sub>2</sub>-consuming capacity due to the presence of MnO<sub>2</sub>, though the intensity remained higher than the untreated group due to the absence of H<sub>2</sub>O<sub>2</sub> exposure in the latter (Fig. 3d, e, g).

NO is an essential regulatory gas molecule within the body, known for its beneficial effects. However, an uncontrolled release of NO can be detrimental to impaired tissues [38]. Therefore, we designed dual-layer microneedles with intelligent NO release. To examine the NO generation at the cellular level, we detected NO using the DAF-FM probe kit. The intensity of green fluorescence was significantly higher in the MN-O<sub>2</sub>/NO group (Fig. 3i). This indicated that the NO donor can generate NO, which was detectable in the cytoplasm of PC12 cells and HUVECs. FCM analysis demonstrated a distinct peak in the MN-O<sub>2</sub>/NO group, confirming the effectiveness of NO-releasing (Fig. 3j). Quantitate analyses aligned with the observation, showing a significant increase of NO fluorescence in PC12 cells and HUVECs (Fig. 3h–k). Additionally, O<sub>2</sub> generation was confirmed using a specific probe that was quenched by O<sub>2</sub>. The red fluorescence [Ru(dpp)<sub>3</sub>Cl<sub>2</sub>] remarkably vanished in MN-O<sub>2</sub>

and MN-O<sub>2</sub>/NO groups, suggesting the generation of O<sub>2</sub> in both groups due to the presence of MnO<sub>2</sub> (Fig. 3l). FCM analysis also illustrated the decreased fluorescence in MN-O<sub>2</sub> and MN-O<sub>2</sub>/NO groups which were quenched by O<sub>2</sub> (Fig. 3m). Quantitative analyses reconfirmed these results in PC12 cells and HUVECs (Fig. 3n; Fig. S11). Collectively, these results confirmed that the MN-O<sub>2</sub> and MN-O<sub>2</sub>/NO can effectively scavenge H<sub>2</sub>O<sub>2</sub> and generate O<sub>2</sub>, thereby improving the microenvironment for wound healing.

#### 3.4. MN-O<sub>2</sub>/NO induced nerve regeneration and regulated the behavior of HUVECs

Diabetic wounds are characterized by reduced neurotrophic function as a result of peripheral nerve impairment and tissue hypoxia stemming from vascular dysfunction [39]. Traditional treatment strategies predominantly focus on promoting angiogenesis or improving oxygenation, often through the addition of inorganic materials such as calcium carbonate or microorganisms like cyanobacteria [40,41]. Recent studies have highlighted that nerve regeneration can accelerate diabetic wound



healing, presenting a new therapeutic avenue [10,16]. Notably, NO has been shown to facilitate nerve regeneration and enhance angiogenesis [23]. To clarify whether MN-O<sub>2</sub>/NO can promote nerve regeneration, PC12 cells were co-cultured with different microneedles. The cells were exposed to a medium containing 10 ng/mL nerve growth factor (NGF) to initiate neural differentiation and 100 μM H<sub>2</sub>O<sub>2</sub> to simulate diabetic microenvironment. The neurite outgrowth of PC12 cells was assessed by evaluating the number of neurite-bearing cells in a Confocal laser scanning microscope (CLMS). Following three days of co-culture, PC12 cell morphology was observed via immunofluorescence with an antibody against β-actin (Fig. 4a). In the MN-O<sub>2</sub> and MN-O<sub>2</sub>/NO groups, a significant increase in neurite outgrowth was observed, demonstrating the efficacy of O<sub>2</sub> and NO in promoting neural differentiation. The degree of neurite outgrowth was classified into three levels according to

the ratio of cellular body to axon length (L0, L1, and L2) (Fig. 4b). The MN-O<sub>2</sub> and MN-O<sub>2</sub>/NO groups showed a significantly higher proportion of neurite-bearing cells compared to other groups, indicating a superior capacity for accelerating nerve regeneration. Compared to the MN group, the MN-O<sub>2</sub> group promoted neural differentiation in L0, L1, and L2, indicating the beneficial effects of ROS scavenging and O<sub>2</sub> supplement. Additionally, MN-O<sub>2</sub>/NO facilitated more pronounced neurite outgrowth than MN-O<sub>2</sub> alone at all levels, demonstrating that NO played a crucial and advantageous role in neurogenesis (Fig. 4c). Furthermore, the average neurite length was also significantly higher when the NO donor was added to the microneedles, suggesting NO can induce longer neurite-bearing cells (Fig. 4d). The levels of neurite outgrowth proteins (NF and GAP43) also increased in the MN-O<sub>2</sub>/NO group compared to other groups, highlighting the role of NO (Fig. 4e; Fig. S12).

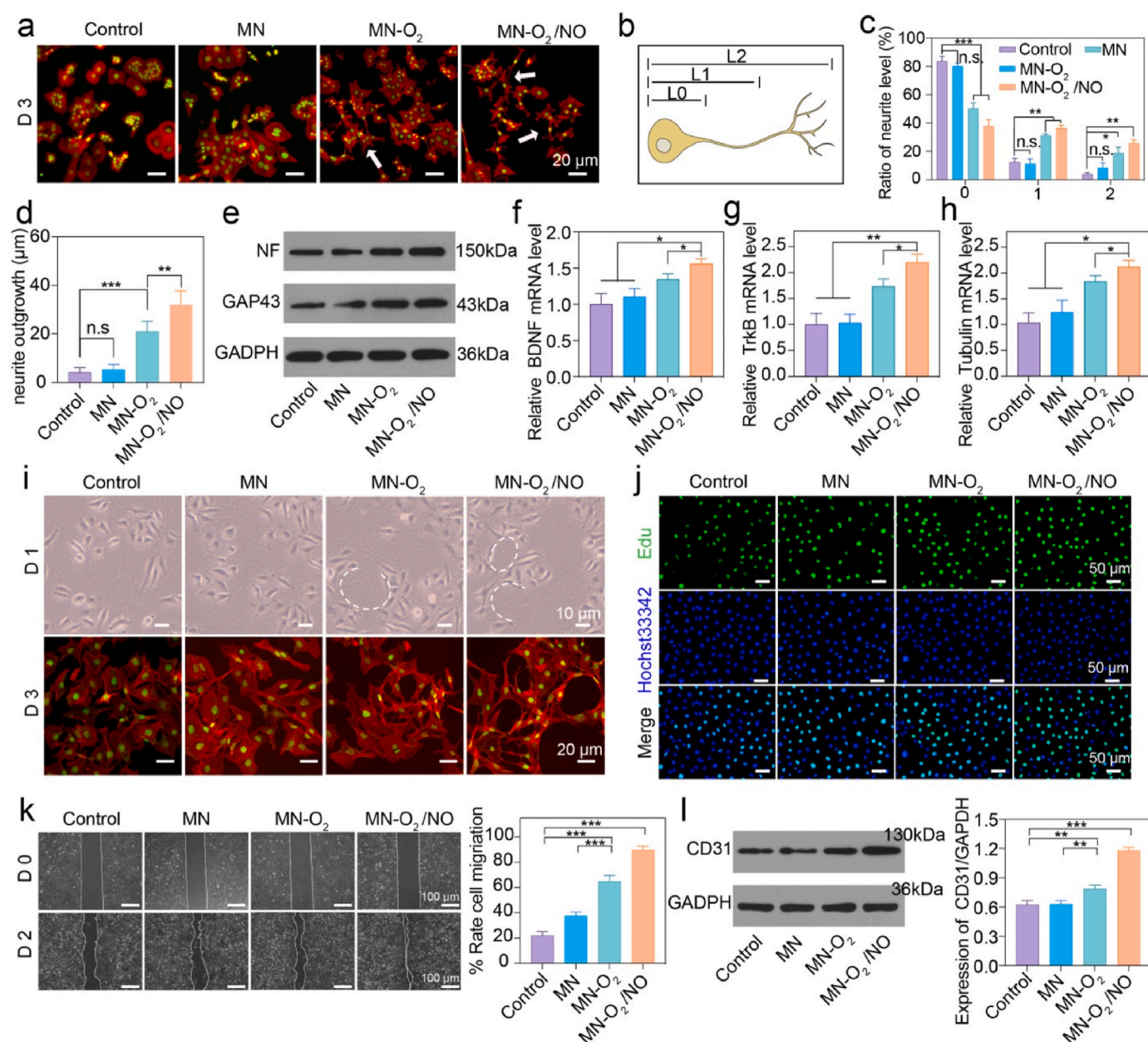


**Fig. 4.** *In vitro* enhancement of nerve extension in PC12 cells and function in HUVECs by microneedles. a) CLMS images of PC12 cell morphology with different microneedles. b) The level of neurite length. The ratio c) and the average length d) of neurite outgrowth. e) Western blotting analysis of NF and GAP43 protein. The qPCR analysis of neurite outgrowth-specific gene expression, including BDNF f), TrkB g), and Tubulin h). i) Representative images of HUVECs with different functionalized microneedles. j) Edu staining analysis of HUVECs. k) Migration ability of HUVECs and quantitative analysis. l) Western blotting analysis of CD31 protein and quantitative analysis. n = 3. Data are represented as mean values ± SD.

Correspondingly, the expression of specific genes involved in neurite outgrowth (BDNF, TrkB, and Tubulin) was upregulated in MN-O<sub>2</sub> and MN-O<sub>2</sub>/NO groups, especially in the latter, aligning with the above findings (Fig. 4f, g, h).

Simultaneously, we examined the biological functionality of micro-needles on HUVECs. The formation of tube-like structures is a fundamental aspect of neovascularization, which also facilitates nerve regeneration. As illustrated in Fig. 4i, HUVECs appeared a spindle-like and elongated morphology at 24h in both the MN-O<sub>2</sub> and MN-O<sub>2</sub>/NO groups. After three days of incubation, well-defined vascular structures can be observed, especially in the MN-O<sub>2</sub>/NO group. In the tube formation assay, more branches and intact tubules were observed in the MN-O<sub>2</sub>/NO group at 6 h (Figure S13). These demonstrated that O<sub>2</sub> generation can enhance angiogenesis, while the release of NO from MN-O<sub>2</sub>/NO can further promote this process. Effective proliferation and migration capacities are essential for HUVECs during all stages of the wound-healing process. EdU assays revealed a higher percentage of HUVECs with green fluorescence in the MN-O<sub>2</sub>/NO group, suggesting that while oxygen can promote endothelial cell proliferation, NO can further enhance this effect (Fig. 4j). Additionally, scratch assays illustrated that the lateral migration ability of HUVECs was significantly improved in the MN-O<sub>2</sub>/NO group (Fig. 4k). Therefore, the incorporation of functional gases can promote superior angiogenesis, migration, and proliferation, which are beneficial for diabetic wound repair. The

protein level of CD31, an endothelial marker, was anticipated to be highest in the MN-O<sub>2</sub>/NO group (Fig. 4l), corroborating the enhanced angiogenic potential.

### 3.5. MN-O<sub>2</sub>/NO promoted neuro-angiogenesis in a Co-culture system

Wound healing encompasses the synergistic processes of neurogenesis and angiogenesis. To further investigate the role of MN-O<sub>2</sub>/NO in cellular intercommunication, we co-cultured PC12 cells and HUVECs for 10 days. Subsequently, immunofluorescent staining for neurological and vascular biomarkers was conducted. As shown in Fig. 5a, red fluorescence in PC12 cells and green fluorescence in HUVECs were detected by CLSM in all groups, indicating  $\beta$ -tubulin and CD31 expression. Notably, the MN-O<sub>2</sub>/NO group exhibited higher fluorescence in both PC12 cells and HUVECs, indicating enhanced expression of proteins specific to neurogenesis and angiogenesis induced by NO delivery. Additionally, more neurite outgrowth was observed in the MN-O<sub>2</sub>/NO group compared to the MN-O<sub>2</sub> group, indicating enhanced synergistic effects of O<sub>2</sub> and NO, consistent with previous results. The schematic diagram of the co-culture is shown in Fig. 5b. Furthermore, qPCR analyses revealed that the expression levels of genes associated with neurogenesis and angiogenesis (BDNF, TrkB, VEGF, and VEGFR2) were significantly elevated in the MN-O<sub>2</sub>/NO group, approximately 1.5–2.5 times higher than those in the control groups. (Fig. 5c–f). Oxygen

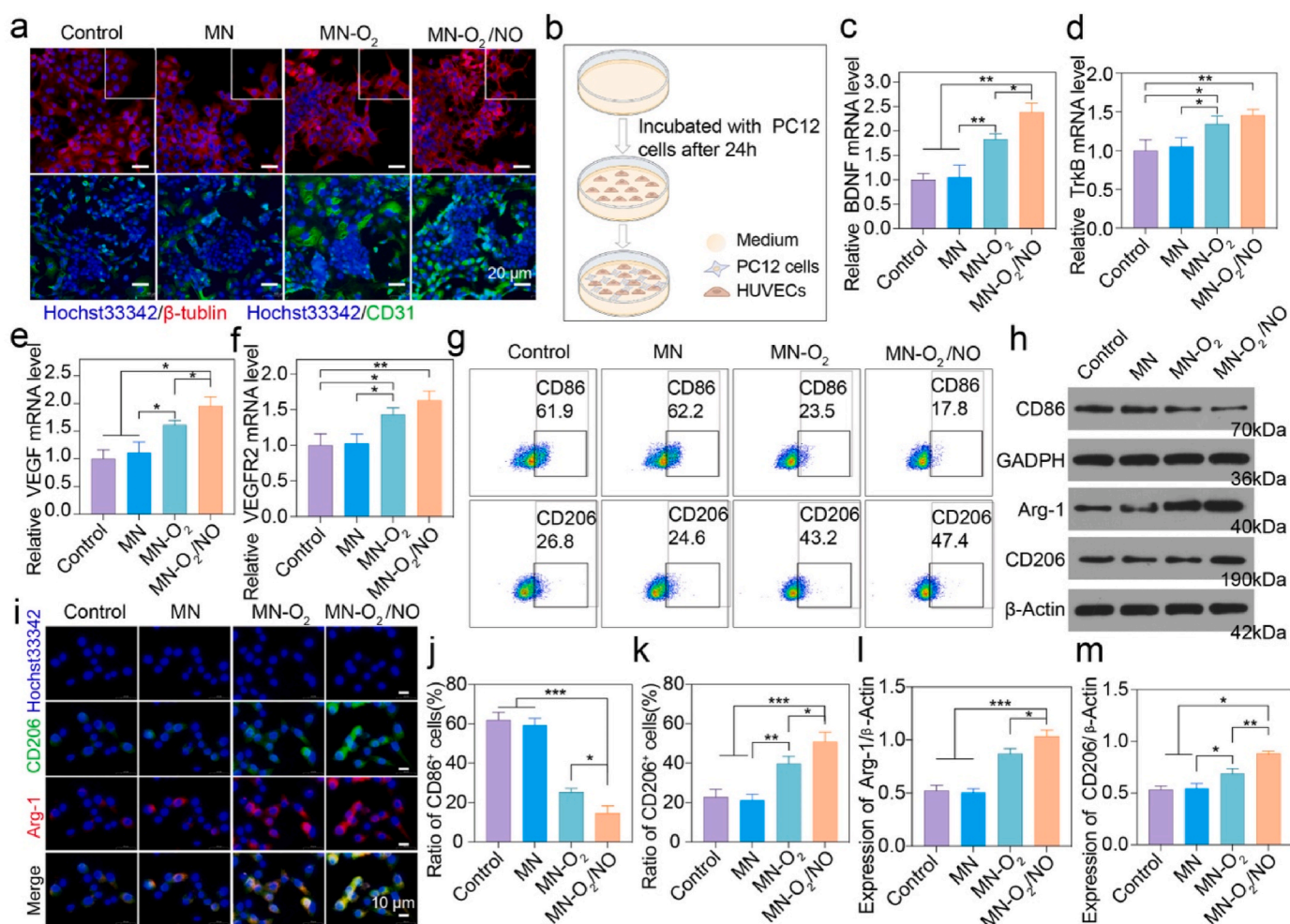


**Fig. 5.** *In vitro* promoted neuro-angiogenesis and regulatory macrophage re-polarization. a) Immunofluorescence staining for  $\beta$ -tubulin (red), CD31 (green), and nucleus (blue) for 10 days co-culture. b) the scheme of the co-culture model. The qPCR analysis of gene expression in BDNF c), TrkB d), VEGF e), and VEGFR2 f). g) FCM analysis of macrophage polarization by detecting CD86 and CD206. h) The Western blotting analyses of M1 and M2 marker proteins. i) Immunofluorescence staining of Arg-1 and CD206 proteins. Quantitative analysis of the ratio of CD86<sup>+</sup> j) and CD206<sup>+</sup> k) macrophages. Quantitative analysis of the expression level of Arg-1 l) and CD206 m) proteins. n = 3. Data are represented as mean values  $\pm$  SD.

delivery enhanced the expression of specific genes by approximately 1.5 times compared to the control and MN groups, whereas in the MN-O<sub>2</sub>/NO group, this result was up to 2 times. These results confirmed that MN-O<sub>2</sub>/NO facilitated neuron-endothelium interaction by upregulating the expression of genes and proteins involved in neurogenesis and angiogenesis.

### 3.6. MN-O<sub>2</sub>/NO facilitated macrophage reprogramming

An anti-inflammatory microenvironment can expedite the inflammatory phase, facilitating its transition to the proliferative phase in diabetic wound healing. Therefore, we investigated the macrophage reprogramming capabilities of MN-O<sub>2</sub>/NO by examining its regulatory function on macrophage polarization *in vitro*. CD86 is recognized as a marker for M1 macrophages, while CD206 is indicative of M2 macrophages. FCM analysis demonstrated that there were fewer M1

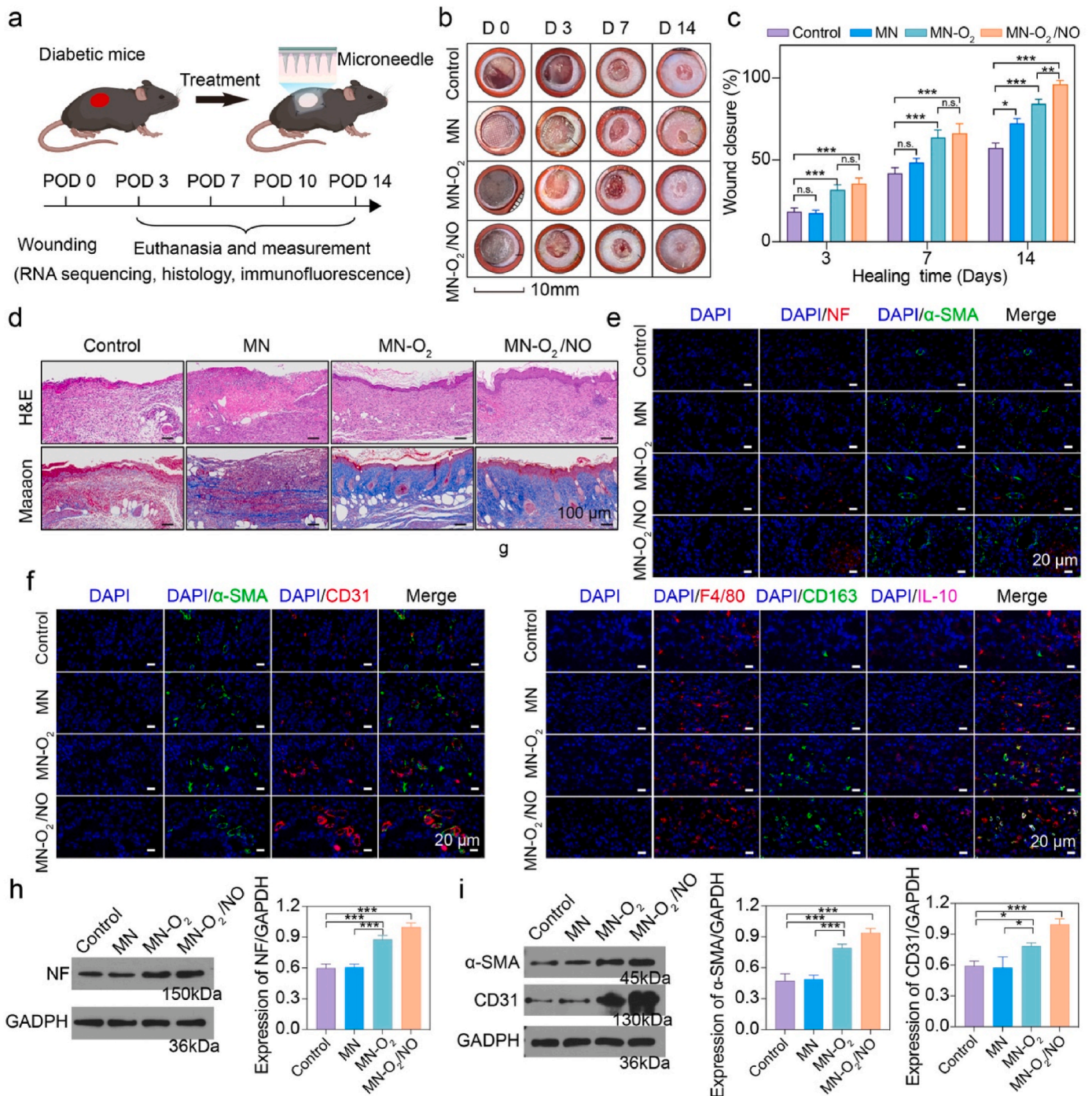


**Fig. 6.** *In vivo* accelerated diabetic wound repair. a) Schematic diagram of experimental design of the spontaneous diabetic mouse wound model. POD: post-operation day. b) Representative images of the wound on days 0, 3, 7, and 14. Wound diameter = 8 mm. c) Quantitative analysis of wound closure rate (n = 5). d) H&E staining and Masson staining of wound tissues on day 14. Representative images of immunofluorescent staining image of neural regeneration e), angiogenesis f), and immune regulation g). Western blotting of proteins specific to nerve regeneration h) and angiogenesis i) and quantitative analyses. Data are represented as mean values ± SD.

macrophages and more M2 macrophages in the MN-O<sub>2</sub>/NO groups (Fig. 5g). This indicated that MN-O<sub>2</sub>/NO can effectively facilitate M2 macrophages repolarization compared to the control, MN, and MN-O<sub>2</sub> groups. Western blotting analysis showed that the protein levels of CD206 and Arg-1, markers for M2 macrophages, were also increased in the MN-O<sub>2</sub>/NO group, while the protein level of CD86, markers for M1 macrophages, was decreased (Fig. 5h, Fig. S14). As shown in Fig. 5i, high fluorescence levels of CD206 and Arg-1 were observed in the MN-O<sub>2</sub>/NO group, indicating enhanced polarization towards the M2 phenotype. Morphologically, reprogrammed macrophages in the MN-O<sub>2</sub>/NO group appeared as elongated spindles with lengths significantly greater than their widths, indicating successful macrophage repolarization induced by gas delivery. And the ability of MN-O<sub>2</sub>/NO to induce M2 macrophage polarization was greater than that of MN-O<sub>2</sub> alone and was more than twice as high as in the control group, according to FCM quantitative analyses (Fig. 5j and k). The protein levels of CD206 and Arg-1 in M2 macrophages were also significantly increased in the MN-O<sub>2</sub>/NO group compared to other groups, affirming that MN-O<sub>2</sub>/NO can efficiently facilitate polarization of macrophages towards the anti-inflammatory M2 phenotype (Fig. 5l and m).

### 3.7. MN-O<sub>2</sub>/NO accelerated diabetic wound healing *in vivo*

To investigate the therapeutic efficiency of MN-O<sub>2</sub>/NO, a full-thickness wound defect was created in spontaneous diabetic mice. The experimental design is depicted in Fig. 6a. To minimize wound movement, we immobilized the wounds to reduce contraction. By the third day, all wounds had decreased in size, indicating an inherent healing ability in the diabetic wounds. By the seventh day, wound sizes in the MN-O<sub>2</sub> and MN-O<sub>2</sub>/NO groups were significantly smaller compared to the control and MN groups, suggesting that the ROS scavenging and oxygen delivery capabilities of the microneedles facilitated wound healing. By the fourteenth day, the MN-O<sub>2</sub>/NO group exhibited the most significant healing, primarily due to the effects of NO, which may promote neurogenesis, as nerve regeneration is slower than angiogenesis. Additionally, wounds in the MN group showed better healing than in the control group, indicating that substances like TA in the MN also contributed to the healing of diabetic wounds. The wound closure rate in the MN-O<sub>2</sub>, MN, and the control was comparatively lower than that in the MN-O<sub>2</sub>/NO group at day 14, indicating the superior wound healing acceleration provided by MN-O<sub>2</sub>/NO (Fig. 6b and c). Then histological evaluation was performed 14 days post-operation using H&E and Masson staining. Although microneedles are beneficial for wound healing, their biocompatibility *in vivo* cannot be overlooked, as it is crucial for the further clinical application [42]. No differences were observed in the H&E staining of the heart, lung, liver, kidney, and spleen, indicating excellent biocompatibility of all microneedle formulations (Fig. S15). In wound tissues, the MN-O<sub>2</sub> and MN-O<sub>2</sub>/NO groups exhibited better epidermal integrity, consistent with the wound closure observations. Moreover, diabetic wounds treated with MN-O<sub>2</sub>/NO demonstrated reduced inflammatory infiltration and increased collagen deposition, indicating an immunoregulatory effect (Fig. 6d).

To further evaluate neurogenesis, angiogenesis, and macrophage reprogramming in wound tissues, we conducted immunofluorescence analysis. As shown in Fig. 6e, NF (red fluorescence) and  $\alpha$ -SMA (green fluorescence) marked newborn nerves and vessels in the wounds, with their intensity being more prominent in the MN-O<sub>2</sub> and MN-O<sub>2</sub>/NO groups than in other groups, indicating promoted concurrent nerve and vessel formation by O<sub>2</sub> delivery. More intact nerves and blood vessels were observed in the MN-O<sub>2</sub>/NO group compared to other groups, suggesting that the synergistic supplementation of O<sub>2</sub> and NO enhanced neurogenesis and angiogenesis. Similarly, the intensity of CD31 and  $\alpha$ -SMA fluorescence was also higher in the MN-O<sub>2</sub>/NO group, as shown in Fig. 6f. Macrophage polarization, crucial for diabetic wound healing, was also evaluated. Red fluorescence (F4/80) indicated immune infiltration in all groups. However, the fluorescence intensity of M2

macrophage biomarkers (CD163 and IL-10) was significantly higher in the MN-O<sub>2</sub> and MN-O<sub>2</sub>/NO groups, indicating a greater proportion of M2 macrophages (Fig. 6g). Moreover, the MN-O<sub>2</sub>/NO group exhibited higher CD163 signals, suggesting that the combined effect of oxygen and NO induced more M2 macrophages, potentially enhancing wound healing. The specific protein levels of NF, CD31, and  $\alpha$ -SMA were also upregulated the most in the MN-O<sub>2</sub>/NO group, aligning with these aforementioned findings (Fig. 6h and i). Hence, these results demonstrated that MN-O<sub>2</sub>/NO can better accelerate diabetic wound healing by promoting nerve regeneration, angiogenesis, and immune reprogramming through O<sub>2</sub> and NO delivery.

### 3.8. The potential mechanism of accelerated diabetic wound healing by MN-O<sub>2</sub>/NO

To elucidate the potential mechanisms underlying the enhanced diabetic wound healing process, we conducted mRNA sequencing analysis on samples from both the control group and MN-O<sub>2</sub>/NO treated group on day 10. As shown in Fig. 7a, Principal Components Analysis (PCA) demonstrated distinct clustering between the control and treated groups, indicating significant differences in their gene expression profiles. Indeed, differential expression gene (DEG) analysis identified 615 up-regulated genes and 740 down-regulated genes in the MN-O<sub>2</sub>/NO treated group compared to the control group (Fig. 7b). A heatmap depicted the expression levels of all DEGs (Fig. 7c). To further delineate the biological process involved, KEGG analysis was performed with up-regulated and down-regulated genes, respectively. Fig. 7d showed enrichment in several classical pathways associated with diabetic wound healing. For instance, in organismal systems, the PPAR signaling pathway regulates essential body metabolism, including in glucolipid, and inhibits inflammation [43,44]. Axon guidance was also enriched, reaffirming the promotion of MN-O<sub>2</sub>/NO on nerve regeneration. In the category of environmental information processing, up-regulated genes were enriched in the Wnt signaling pathway, mTOR signaling pathway, and ECM-receptor interaction, all of which are beneficial for diabetic wound healing. The Wnt signaling pathway involves complex signal transduction processes that influence cell proliferation, differentiation, and apoptosis [45,46]. mTOR is an atypical serine/threonine protein kinase that plays an important role in apoptosis, autophagy, and metabolism [47]. Studies have shown that activation of mTOR can promote axon regeneration [48,49]. ECM-receptor interaction is well known to promote cell adhesion and migration, which is advantageous for wound healing [50,51]. Conversely, numerous immune-related pathways were down-regulated, aligning with the immunomodulatory effects *in vitro* (Fig. 7e). Gene Ontology (GO) analysis also confirmed that DEGs were associated with immunity and many signaling transduction processes (Fig. 7f). Additionally, Gene Set Enrichment Analysis (GSEA) revealed significant enrichment of the VEGF signaling pathway, highlighting the angiogenic effects of MN-O<sub>2</sub>/NO (Fig. 7g). In summary, transcriptome sequencing revealed that MN-O<sub>2</sub>/NO enhanced diabetic wound healing by promoting nerve regeneration, modulating immune responses, and stimulating angiogenesis. These processes were primarily mediated through key pathways, including axon guidance, mTOR signaling, PPAR signaling, Wnt signaling, and VEGF signaling.

### 3.9. Mechanistic validation of accelerated diabetic wound healing

We further validated the expression of key DEGs in the pathways of immune modulation, axon guidance, and vascular generation. The expression levels of these genes from RNA-Seq are presented in Fig. 8a. In the qPCR analysis, the expression of inflammation-related genes (Tnf and Il1b) decreased in the MN-O<sub>2</sub>/NO group, while genes associated with nerve regeneration (Robo2 and Sema3c) and vascular generation (Vegfa) showed increased expression (Fig. 8b). Additionally, previous pathway analyses indicated that the mTOR pathway was enriched, which was closely related to tissue repair. Activation of the PI3K-AKT-

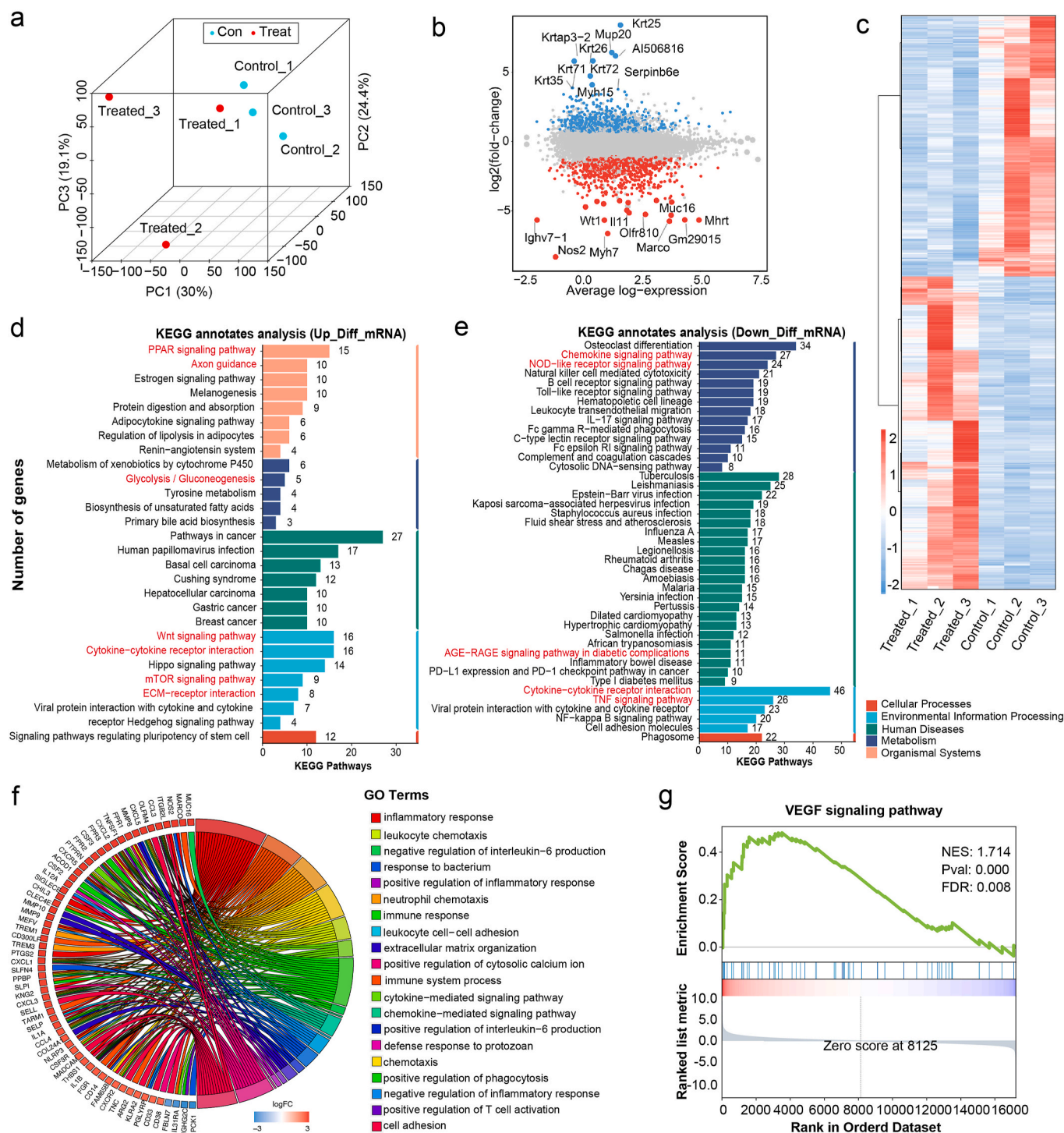


**Fig. 7.** Transcriptomic analysis for potential mechanisms. a) PCA analysis of the control and MN-O<sub>2</sub>/NO groups. The volcano b) and heatmap c) of DEGs. KEGG enrichment of up-regulated d) and down-regulated e) genes. Diabetic-related pathways highlighted in red. f) GO analysis of DEGs in biological processes. g) GSEA enrichment pathways.

mTOR signaling pathway can promote neuronal survival and axonal regeneration [52–54], as well as angiogenesis [55,56] and immune modulation [57,58]. The protein expression levels of p-mTOR, p-AKT, and p-PI3K were significantly elevated, indicating the activation of the PI3K-AKT-mTOR pathway in diabetic wounds treated with MN-O<sub>2</sub> and MN-O<sub>2</sub>/NO, particularly in the latter (Fig. 8c and d). The classical mTOR pathway was often associated with the process of autophagy, further promoting cellular self-repair. Immunofluorescence results demonstrated that LC3 protein expression was markedly higher in the

MN-O<sub>2</sub>/NO group compared to the MN-O<sub>2</sub> and control groups, indicating a greater occurrence of autophagy (Fig. 8e). Similarly, transmission electron microscopy results of wound tissues also revealed a higher presence of autophagosomes in the MN-O<sub>2</sub>/NO group (Fig. 8f). Previous studies have reported that nitric oxide administration during liver ischemia-reperfusion can activate autophagy to protect tissue damage [59]. Nevertheless, the PI3K-AKT-mTOR pathway primarily participates in intracellular signaling processes. VEGFR2, an important cell membrane receptor, plays a crucial role in promoting the activation

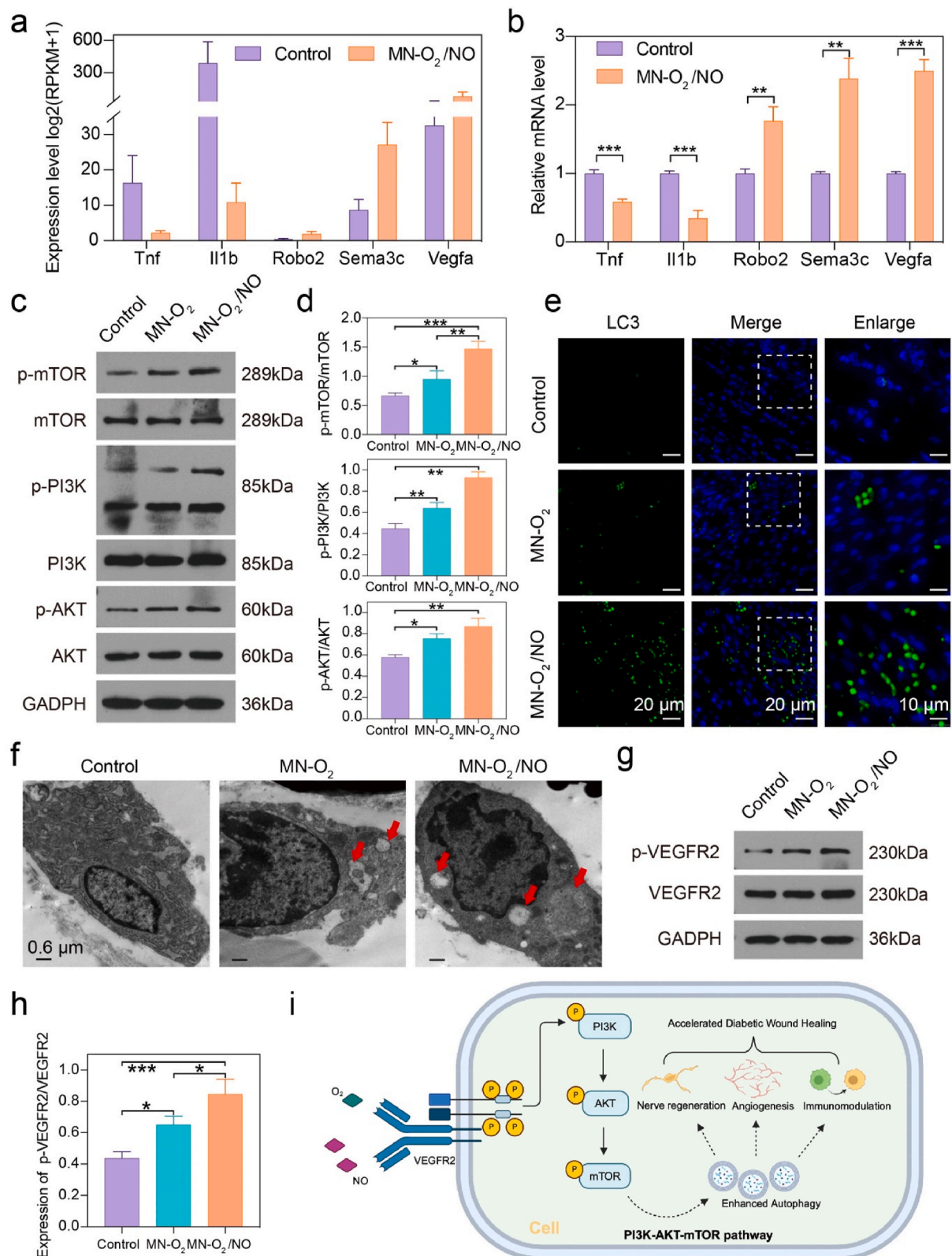


**Fig. 8.** Further investigation of the potential mechanisms. a) The expression level of key genes in the control and MN-O<sub>2</sub>/NO groups by RNA-Seq a) and qPCR b). The protein expression level of PI3K-AKT-mTOR pathway c) and quantitative analyses d). e) Representative images of immunofluorescent staining image of LC protein. f) transmission electron microscopy images of autophagosomes. The protein expression level of p-VEGFR2 and VEGFR2 g) and quantitative analysis h). i) The Mechanism diagram of intracellular activation. n = 3. Data are represented as mean values ± SD.

of the downstream PI3K-AKT signaling pathway, thereby enhancing cell survival and growth; studies have shown its expression across various cell types [60]. The protein expression level of p-VEGFR2 increased in the MN-O<sub>2</sub>/NO group compared to the MN-O<sub>2</sub> and control groups, suggesting its involvement in the modulation of wound healing (Fig. 8g and h). Therefore, multifunctional microneedles may potentially promote nerve regeneration, angiogenesis, and immune modulation by enhancing VEGFR2 activation, which in turn further activates the PI3K-AKT-mTOR pathway to facilitate autophagy, ultimately accelerating the healing of diabetic wounds (Fig. 8i).

#### 4. Conclusion

In our study, we developed a dual-layer multifunctional micro-needle, with an inner layer containing a synthetic donor for supplying NO and an outer layer incorporating MnO<sub>2</sub> to scavenge ROS and generate O<sub>2</sub>, connected by phenylborate esters. This design enabled the gradual release of O<sub>2</sub> and NO for diabetic wound treatment, demonstrating potential in combining anti-oxidation, neurogenesis, angiogenesis, and immunomodulation to comprehensively accelerate diabetic wound healing. Furthermore, the strategy of using microneedles for the sequential release of therapeutic gases provides critical insights into the field of regeneration.

#### CRediT authorship contribution statement

**Changjiang Liu:** Writing – review & editing, Writing – original draft, Methodology, Formal analysis, Data curation, Conceptualization. **Kun Liu:** Writing – review & editing, Writing – original draft, Methodology, Formal analysis, Data curation, Conceptualization. **Dong Zhang:** Writing – review & editing, Writing – original draft, Methodology, Formal analysis, Data curation, Conceptualization. **Yuting Liu:** Investigation, Formal analysis. **Yifeng Yu:** Methodology, Investigation. **Haifei Kang:** Investigation. **Xianzhen Dong:** Methodology. **Honglian Dai:** Writing – review & editing, Supervision, Resources, Project administration, Funding acquisition, Conceptualization. **Aixi Yu:** Writing – review & editing, Supervision, Resources, Project administration, Funding acquisition, Conceptualization.

#### Data availability

Data will be made available on request.

#### Ethics approval and consent to participate

All the animal experiments were implemented according to the guidelines for laboratory animals established by the Wuhan University Center for Animal Center Experiment/A3-Lab. All mouse experiments were approved by the Institutional Animal Care and Utilization Committee (IACUC) of the Animal Experiment Center of Wuhan University (Approval number: WP20230029).

#### Declaration of competing interest

The authors declare that they have no known competing financial interests or personal relationships that could have appeared to influence the work reported in this paper.

#### Acknowledgements

This work was supported by grants from the National Natural Science Foundation of China (52372272, 32201109, 82072440), Zhongnan Hospital of Wuhan University, Excellent Doctor Fund Project (ZNYB2022015), Natural Science Foundation of Hubei Province (2024AFD167), and the Basic and Applied Basic Research Foundation of Guangdong Province (2022B1515120052, 2021A1515110557). All the

animal experiments were implemented according to the guidelines for laboratory animals established by the Wuhan University Center for Animal Center Experiment/A3-Lab. All mouse experiments were approved by the Institutional Animal Care and Utilization Committee (IACUC) of the Animal Experiment Center of Wuhan University (Approval number: WP20230029).

#### Appendix A. Supplementary data

Supplementary data to this article can be found online at <https://doi.org/10.1016/j.bioactmat.2024.12.012>.

#### References

- [1] N. Singh, D.G. Armstrong, B.A. Lipsky, Preventing foot ulcers in patients with diabetes, *JAMA* 293 (2) (2005) 217–228.
- [2] S. Maschalidi, P. Mehrotra, B.N. Keceli, H.K.L. De Cleene, K. Lecomte, R. Van der Cruyssen, P. Janssen, J. Pinney, G. van Loo, D. Elewaut, A. Massie, E. Hoste, K. S. Ravichandran, Targeting SLC7A11 improves efferocytosis by dendritic cells and wound healing in diabetes, *Nature* 606 (7915) (2022) 776–784.
- [3] E.L. Feldman, B.C. Callaghan, R. Pop-Busui, D.W. Zochodne, D.E. Wright, D. L. Bennett, V. Bril, J.W. Russell, V. Viswanathan, Diabetic neuropathy, *Nat. Rev. Dis. Prim.* 5 (1) (2019) 41.
- [4] A.M. Tataru, D.P. Kontoyiannis, A.G. Mikos, Drug delivery and tissue engineering to promote wound healing in the immunocompromised host: current challenges and future directions, *Adv. Drug Deliv. Rev.* 129 (2018) 319–329.
- [5] Y. Zhao, M.X. Li, J.Y. Mao, Y.H. Su, X. Huang, W.Z. Xia, X.F. Leng, T. Zan, Immunomodulation of wound healing leading to efferocytosis, *Smart Med* 3 (1) (2024).
- [6] Y.N. Qian, C.C. Xu, W. Xiong, N. Jiang, Y.J. Zheng, X.J. He, F. Ding, X.H. Lu, J. L. Shen, Dual cross-linked organic-inorganic hybrid hydrogels accelerate diabetic skin wound healing, *Chem. Eng. J.* 417 (2021).
- [7] X.L. Qi, E. Cai, Y.J. Xiang, C.F. Zhang, X.X. Ge, J.J. Wang, Y.L. Lan, H.B. Xu, R. D. Hu, J.L. Shen, An immunomodulatory hydrogel by hyperthermia-assisted self-cascade glucose depletion and ROS scavenging for diabetic foot ulcer wound therapeutics, *Adv. Mater.* 35 (48) (2023).
- [8] K. Las Heras, I. Garcia-Orue, F. Rancan, M. Igartua, E. Santos-Vizcaino, R. M. Hernandez, Modulating the immune system towards a functional chronic wound healing: a biomaterials and Nanomedicine perspective, *Adv. Drug Deliv. Rev.* 210 (2024) 115342.
- [9] D.G. Greenhalgh, Basic techniques for optimizing burn wound healing: insights from clinical practice, *Plast. Aesthet. Res.* 11 (2024).
- [10] Y.Z. Lu, B. Nayer, S.K. Singh, Y.K. Alshoubaki, E. Yuan, A.J. Park, K. Maruyama, S. Akira, M.M. Martino, CGRP sensory neurons promote tissue healing via neutrophils and macrophages, *Nature* 628 (8008) (2024) 604–611.
- [11] L.H. Peng, X.H. Xu, Y.F. Huang, X.L. Zhao, B. Zhao, S.Y. Cai, M.J. Xie, M.Z. Wang, T.J. Yuan, Y. He, Z. Xu, J.Q. Gao, C. Gao, Self-adaptive all-in-one delivery chip for rapid skin nerves regeneration by endogenous mesenchymal stem cells, *Adv. Funct. Mater.* 30 (40) (2020).
- [12] Y. Xiong, Z. Lin, P. Bu, T. Yu, Y. Endo, W. Zhou, Y. Sun, F. Cao, G. Dai, Y. Hu, L. Lu, L. Chen, P. Cheng, K. Zha, M.A. Shahbazi, Q. Feng, B. Mi, G. Liu, A whole-course-repair system based on neurogenesis-angiogenesis crosstalk and macrophage reprogramming promotes diabetic wound healing, *Adv. Mater.* 35 (19) (2023) e2212300.
- [13] X.H. Fu, J. Wang, D.J. Qian, Z.W. Chen, L. Chen, W.G. Cui, Y. Wang, Living electrospun short fibrous sponge via engineered nanofat for wound healing, *Adv. Fiber Mater.* 5 (3) (2023) 979–993.
- [14] X.H. Fu, J. Wang, D.J. Qian, L.H. Xi, L. Chen, Y.W. Du, W.G. Cui, Y. Wang, Oxygen atom-concentrating short fibrous sponge regulates cellular respiration for wound healing, *Adv. Fiber Mater.* 5 (5) (2023) 1773–1787.
- [15] N.P. Gonçalves, C.B. Vægter, H. Andersen, L. Ostergaard, N.A. Calcutt, T.S. Jensen, Schwann cell interactions with axons and microvessels in diabetic neuropathy, *Nat. Rev. Neurol.* 13 (3) (2017) 135–147.
- [16] H. Majd, S. Amin, Z. Ghazizadeh, A. Cesulius, E. Arroyo, K. Lankford, A. Majd, S. Farahvashi, A.K. Chemel, M. Okoye, M.D. Scantlen, J. Tchiew, E.L. Calder, V. Le Rouzic, B. Shibata, A. Arab, H. Goodarzi, G. Pasternak, J.D. Kocsis, S.B. Chen, L. Studer, F. Fattahi, Deriving Schwann cells from hPSCs enables disease modeling and drug discovery for diabetic peripheral neuropathy, *Cell Stem Cell* 30 (5) (2023), 632+.
- [17] J.Y. Ding, K. Xu, H.T. Xu, J.S. Ji, Y.N. Qian, J.L. Shen, Advances in gas therapeutics for wound healing: mechanisms, delivery materials, and prospects, *Small Struct.* 5 (1) (2024).
- [18] A.K. Barui, S.K. Nethi, C.R. Patra, Investigation of the role of nitric oxide driven angiogenesis by zinc oxide nanoflowers, *J. Mater. Chem. B* 5 (18) (2017) 3391–3403.
- [19] C.V. Suschek, D. Feibel, M. von Kohout, C. Oplander, Enhancement of nitric oxide bioavailability by modulation of cutaneous nitric oxide stores, *Biomedicines* 10 (9) (2022).
- [20] Y. Guan, H. Niu, Z. Liu, Y. Dang, J. Shen, M. Zayed, L. Ma, J. Guan, Sustained oxygenation accelerates diabetic wound healing by promoting epithelialization and angiogenesis and decreasing inflammation, *Sci. Adv.* 7 (35) (2021).

- [21] M.J. Malone-Povolny, S.E. Maloney, M.H. Schoenfisch, Nitric oxide therapy for diabetic wound healing, *Adv. Healthcare Mater.* 8 (12) (2019).
- [22] Y.Z. Zhao, L.Z. Luo, L.T. Huang, Y.Y. Zhang, M.Q. Tong, H.X. Pan, J.X. Shangguan, Q. Yao, S.H. Xu, H.L. Xu, Hydrogel capturing nitric oxide microbubbles accelerates the healing of diabetic foot, *J. Contr. Release* 350 (2022) 93–106.
- [23] J. Park, K. Jin, A. Sahasrabudhe, P.H. Chiang, J.H. Maalouf, F. Koehler, D. Rosenfeld, S. Rao, T. Tanaka, T. Khudiyev, Z.J. Schiffer, Y. Fink, O. Yizhar, K. Manthiram, P. Anikeeva, In situ electrochemical generation of nitric oxide for neuronal modulation, *Nat. Nanotechnol.* 15 (8) (2020), 690–+.
- [24] J.I. Lee, J.H. Park, Y.R. Kim, K. Gwon, H.W. Hwang, G. Jung, J.Y. Lee, J.Y. Sun, J. W. Park, J.H. Shin, M.R. Ok, Delivery of nitric oxide-releasing silica nanoparticles for in vivo revascularization and functional recovery after acute peripheral nerve crush injury, *Neural Regen. Res.* 17 (9) (2022) 2043–2049.
- [25] Y. Guan, H. Niu, Z.T. Liu, Y. Dang, J. Shen, M. Zayed, L. Ma, J.J. Guan, Sustained oxygenation accelerates diabetic wound healing by promoting epithelialization and angiogenesis and decreasing inflammation, *Sci. Adv.* 7 (35) (2021).
- [26] P. Wang, J. Wu, H. Yang, H. Liu, T. Yao, C. Liu, Y. Gong, M. Wang, G. Ji, P. Huang, X. Wang, Intelligent microneedle patch with prolonged local release of hydrogen and magnesium ions for diabetic wound healing, *Bioact. Mater.* 24 (2023) 463–476.
- [27] B. Lin, B. Gao, M. Wei, S. Li, Q. Zhou, B. He, Overexpressed artificial spidroin based microneedle spinneret for 3D air spinning of hybrid spider silk, *ACS Nano* 18 (37) (2024) 25778–25794.
- [28] X. Zhang, J. Gan, L. Fan, Z. Luo, Y. Zhao, Bioinspired adaptable indwelling microneedles for treatment of diabetic ulcers, *Adv. Mater.* 35 (23) (2023) e2210903.
- [29] L. Fan, X.X. Zhang, L. Wang, Y.Z. Song, K.X. Yi, X.J. Wang, H.B. Zhang, L. Li, Y. J. Zhao, Bio-inspired porous microneedles dwelled stem cells for diabetic wound treatment, *Adv. Funct. Mater.* 34 (28) (2024).
- [30] X. Luan, X.X. Zhang, M. Nie, Y.J. Zhao, Traditional Chinese Medicine Integrated Responsive Microneedles for Systemic Sclerosis Treatment, *Research-China* 6, 2023.
- [31] S. Yao, Y. Luo, Y. Wang, Engineered microneedles arrays for wound healing, *Eng. Regen.* 3 (3) (2022) 232–240.
- [32] H.F. Kang, W.Y. Wei, L.S. Sun, R. Yu, E.R. Yang, X.P. Wu, H.L. Dai, Modular design and bonding mechanism of internal boron-nitrogen coordinated boronic ester hydrogels with alkaline pH responsiveness and tunable gelation pH, *Chem. Mater.* 35 (6) (2023) 2408–2420.
- [33] H. Xia, Z. Dong, Q. Tang, R.J. Ding, Y.M. Bai, K. Zhou, L.H. Wu, L.L. Hao, Y.Y. He, J. Yang, H.L. Mao, Z.W. Gu, Glycopeptide-based multifunctional hydrogels promote diabetic wound healing through pH regulation of microenvironment, *Adv. Funct. Mater.* 33 (29) (2023).
- [34] S.Q. Wang, H. Zheng, L. Zhou, F. Cheng, Z. Liu, H.P. Zhang, L.L. Wang, Q.Y. Zhang, Nanoenzyme-reinforced injectable hydrogel for healing diabetic wounds infected with multidrug resistant bacteria, *Nano Lett.* 20 (7) (2020) 5149–5158.
- [35] L.Y. Wang, B.H. Zhu, Y.T. Deng, T.T. Li, Q.Y. Tian, Z.G. Yuan, L. Ma, C. Cheng, Q. Y. Guo, L. Qiu, Biocatalytic and antioxidant nanostructures for ROS scavenging and biotherapeutics, *Adv. Funct. Mater.* 31 (31) (2021).
- [36] Y. Zhao, D.D. Wang, T.W. Qian, J.M. Zhang, Z.H. Li, Q.Y. Gong, X.Z. Ren, Y. L. Zhao, Biomimetic nanozyme-decorated hydrogels with HO-activated oxygenation for modulating immune microenvironment in diabetic wound, *ACS Nano* 17 (17) (2023) 16854–16869.
- [37] Y.Y. Xu, Y.F. Luo, Z.Z. Weng, H.C. Xu, W. Zhang, Q. Li, H.J. Liu, L.B. Liu, Y. M. Wang, X.X. Liu, L. Liao, X.L. Wang, Microenvironment-responsive metal-phenolic nanozyme release platform with antibacterial, ROS scavenging, and osteogenesis for periodontitis, *ACS Nano* 17 (19) (2023) 18732–18746.
- [38] Y.B. Feng, L.F. Su, L. Liu, Z.Y. Chen, Y.C. Ji, Y.W. Hu, D.D. Zheng, Z. Chen, C.B. Lei, H. Xu, Y.C. Han, H.X. Shen, Accurate spatio-temporal delivery of nitric oxide facilitates the programmable repair of avascular dense connective tissues injury, *Adv. Healthcare Mater.* 13 (14) (2024).
- [39] A.M. Vincent, B.C. Callaghan, A.L. Smith, E.L. Feldman, Diabetic neuropathy: cellular mechanisms as therapeutic targets, *Nat. Rev. Neurol.* 7 (10) (2011) 573–583.
- [40] E. Zhao, T. Xiao, Y. Tan, X. Zhou, Y. Li, X. Wang, K. Zhang, C. Ou, J. Zhang, Z. Li, H. Liu, Separable microneedles with photosynthesis-driven oxygen manufactory for diabetic wound healing, *ACS Appl. Mater. Interfaces* 15 (6) (2023) 7725–7734.
- [41] N. Li, X.H. Lu, Y.Y. Yang, S. Ning, Y. Tian, M.Y. Zhou, Z. Wang, L. Wang, J.F. Zang, Calcium peroxide-based hydrogel patch with sustainable oxygenation for diabetic wound healing, *Adv. Healthcare Mater.* 13 (2024).
- [42] A.L. Pignet, A. Hecker, T. Voljc, M. Carmieletto, N. Watzinger, L.P. Kamolz, The use of acellular fish skin grafts in burns and complex trauma wounds: a systematic review of clinical data, *Plast. Aesthet. Res.* 11 (2024).
- [43] C.K. Glass, K. Saijo, Nuclear receptor transrepression pathways that regulate inflammation in macrophages and T cells, *Nat. Rev. Immunol.* 10 (5) (2010) 365–376.
- [44] G. Pascual, A.L. Fong, S. Ogawa, A. Gamliel, A.C. Li, V. Perissi, D.W. Rose, T. M. Willson, M.G. Rosenfeld, C.K. Glass, A SUMOylation-dependent pathway mediates transrepression of inflammatory response genes by PPAR- $\gamma$ , *Nature* 437 (7059) (2005) 759–763.
- [45] T. Saneyoshi, S. Kume, Y. Amasaki, K. Mikoshiba, The Wnt/calcium pathway activates NF-AT and promotes ventral cell fate in embryos, *Nature* 417 (6886) (2002) 295–299.
- [46] H. Tanaka, I. Matsumura, Y. Satoh, S. Ezo, T. Nakahata, Y. Kanakura, Wnt/ $\beta$ -Catenin pathway affects the cell-fate decisions of hematopoietic stem/progenitor cells modulating the epigenetic states of various essential transcription factors, *Blood* 112 (11) (2008) 847, 847.
- [47] V. Panwar, A. Singh, M. Bhatt, R.K. Tonk, S. Azizov, A.S. Raza, S. Sengupta, D. Kumar, M. Garg, Multifaceted role of mTOR (mammalian target of rapamycin) signaling pathway in human health and disease, *Signal Transduct. Tar.* 8 (1) (2023).
- [48] S.E. Thomson, C. Charalambous, C.A. Smith, P.M. Tsimbouri, T. Déjardin, P. J. Kingham, A.M. Hart, M.O. Riehle, Microtopographical cues promote peripheral nerve regeneration via transient mTORC2 activation, *Acta Biomater.* 60 (2017) 220–231.
- [49] J. Fei, S.J. Chen, X.C. Song, Y.H. Liang, K.L. Duan, X.W. Peng, L.J. Li, Exogenous GDNF promotes peripheral facial nerve regeneration in rats through the PI3K/AKT/mTOR signaling pathway, *Faseb. J.* 38 (1) (2024).
- [50] Q. Li, Y.M. Niu, H.J. Diao, L.T. Wang, X.P. Chen, Y.T. Wang, L. Dong, C.M. Wang, Sequestration of endogenous PDGF-BB with an ECM-mimetic sponge for accelerated wound healing, *Biomaterials* 148 (2017) 54–68.
- [51] A. Arin, M.S. Rahaman, U. Farwa, B.T. Lee, Faster and protective wound healing mechanistic of para-coumaric acid loaded liver ECM scaffold cross-linked with acellular marine kelp, *Adv. Funct. Mater.* 33 (17) (2023).
- [52] S. Wu, C. Liu, J. Tang, C. Wu, Q. Zhang, Z. Liu, J. Han, J. Xue, J. Lin, Y. Chen, J. Yang, Y. Zhuo, Y. Li, Tafluprost promotes axon regeneration after optic nerve crush via Zn(2+)-mTOR pathway, *Neuropharmacology* 242 (2024) 109746.
- [53] Y. Zhao, Q. Wang, C. Xie, Y. Cai, X. Chen, Y. Hou, L. He, J. Li, M. Yao, S. Chen, W. Wu, X. Chen, A. Hong, Peptide ligands targeting FGF receptors promote recovery from dorsal root crush injury via AKT/mTOR signaling, *Theranostics* 11 (20) (2021) 10125–10147.
- [54] J. Fei, S. Chen, X. Song, Y. Liang, K. Duan, X. Peng, L. Li, Exogenous GDNF promotes peripheral facial nerve regeneration in rats through the PI3K/AKT/mTOR signaling pathway, *Faseb. J.* 38 (1) (2024) e23340.
- [55] S. Song, G. Zhang, X. Chen, J. Zheng, X. Liu, Y. Wang, Z. Chen, Y. Wang, Y. Song, Q. Zhou, HIF-1 $\alpha$  increases the osteogenic capacity of ADSCs by coupling angiogenesis and osteogenesis via the HIF-1 $\alpha$ /VEGF/AKT/mTOR signaling pathway, *J. Nanobiotechnol.* 21 (1) (2023) 257.
- [56] L. Ma, X. Wang, Y. Zhou, X. Ji, S. Cheng, D. Bian, L. Fan, L. Zhou, C. Ning, Y. Zhang, Biomimetic Ti-6Al-4V alloy/gelatin methacrylate hybrid scaffold with enhanced osteogenic and angiogenic capabilities for large bone defect restoration, *Bioact. Mater.* 6 (10) (2021) 3437–3448.
- [57] S.P. Cobbold, The mTOR pathway and integrating immune regulation, *Immunology* 140 (4) (2013) 391–398.
- [58] J. Wu, Y. Wu, H. Tang, W. Li, Z. Zhao, X. Shi, H. Jiang, L. Yu, H. Deng, Self-adapting biomass hydrogel embodied with miRNA immunoregulation and long-term bacterial eradication for synergistic chronic wound therapy, *ACS Nano* 18 (28) (2024) 18379–18392.
- [59] J.K. Shin, J.W. Kang, S.M. Lee, Enhanced nitric oxide-mediated autophagy contributes to the hepatoprotective effects of ischemic preconditioning during ischemia and reperfusion, *Nitric Oxide* 58 (2016) 10–19.
- [60] M. Simons, E. Gordon, L. Claesson-Welsh, Mechanisms and regulation of endothelial VEGF receptor signalling, *Nat. Rev. Mol. Cell Biol.* 17 (10) (2016) 611–625.